



저작자표시-비영리-변경금지 2.0 대한민국

이용자는 아래의 조건을 따르는 경우에 한하여 자유롭게

- 이 저작물을 복제, 배포, 전송, 전시, 공연 및 방송할 수 있습니다.

다음과 같은 조건을 따라야 합니다:



저작자표시. 귀하는 원저작자를 표시하여야 합니다.



비영리. 귀하는 이 저작물을 영리 목적으로 이용할 수 없습니다.



변경금지. 귀하는 이 저작물을 개작, 변형 또는 가공할 수 없습니다.

- 귀하는, 이 저작물의 재이용이나 배포의 경우, 이 저작물에 적용된 이용허락조건을 명확하게 나타내어야 합니다.
- 저작권자로부터 별도의 허가를 받으면 이러한 조건들은 적용되지 않습니다.

저작권법에 따른 이용자의 권리는 위의 내용에 의하여 영향을 받지 않습니다.

이것은 [이용허락규약\(Legal Code\)](#)을 이해하기 쉽게 요약한 것입니다.

[Disclaimer](#)

공학박사학위논문

**The Fabrication of Functional Surfaces
via Multiscale Deposition Methods**

멀티스케일 증착공정을 이용한 기능성 표면의 제작

2015 년 8 월

서울대학교 대학원

기계항공공학부

김 정 훈

The Fabrication of Functional Surface via Multiscale Deposition Methods

멀티스케일 증착공정을 이용한 기능성 표면의 제작

지도교수 최 만 수

이 논문을 공학박사 학위논문으로 제출함

2015 년 6 월

서울대학교 대학원

기계항공공학부

김 정 훈

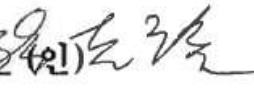
김정훈의 공학박사 학위논문을 인준함

2015 년 6 월

위원장 : 전 누리 (인) 

부위원장 : 최 만수 (인) 

위원 : 고 능환 (인) 

위원 : 손 지원 (인) 

위원 : 정 훈의 (인) 

Abstract

In this thesis, we report novel multiscale deposition methods for fabricating functional surfaces. The processes using polymer and aerosol process have various advantages such as fast, cost-effective, easy material preparation and atmospheric environment process. We fabricated functional surfaces which have selective wettability, controllable wettability and energy conversion properties using those advantages.

First, we present that a thin layer of polydimethyl siloxane (PDMS) in the nano-thickness (< 100 nm) can be generated multiple times (> 10) by utilizing irreversible bonding with oxygen plasma treatment and controlled interfacial fracture. The clean cleavage is attributed to the built-in stress at the fracture interface during the plasma treatment, resulting in the repetitive formation of a smooth membrane of ~5 nm roughness from the bulk PDMS. And then, we controlled height of transferred pattern via oxygen plasma treatment conditions and intrinsic characteristics of PDMS stamp. The method can be used to transfer various micro- and nanopatterns without a residual layer as well as to form nanogrooves of controlled dimension. Also, we achieved highly specific protein immobilization on the patterned surface of a solid substrate in a site-directed manner.

Next, we investigated about magnetic responsive and superhydrophobic pillar

arrays via spray method. The magnetic pillars grow following magnetic field direction during spray process, represent enormous deflection under the magnetic force. From the fabrication result, we analyzed structure change and wetting characteristics of the pillars as strength of magnetic field and number of coating. Size of pillar was increased by repeated coating process and it makes the pillars become more hydrophobic. Furthermore, dual-roughness of pillars dramatically decreased the CA hysteresis of the pillar arrays. The large bending of the pillars generates geometrical potentials decrease the droplet ROAs on the structure. By the active property, we adjust sliding direction of the droplet by orientation of the magnet and we show active droplet manipulation and mixing result on the pillar structure via only structural modulation. Furthermore, formed ice particle under subzero temperature could be removed by motion of the magnetic pillar.

Finally, we present fabrication process to make the components of the solid oxide fuel cell (SOFC) using Electrospray deposition (ESD) method which can deposit a uniform membrane through simple step and evaluated its performances. The components of the SOFC such as anode functional layer (AFL), electrolyte layer, cathode functional layer (CFL) and cathode layer could be fabricated by ESD method followed by annealing process. Especially, we could get dense membrane and porous structure using ESD process. During annealing process, the morphology of the membrane is determined by the amount of the binder. In the low concentration of the binding polymer, the porous membrane is fabricated but

in the high concentration, dense membrane morphology is attained. As a result, we could adjust the morphology of the ceramic membrane via ESD method and the concentration of polymer binder. Structure of cathode and electrolyte was optimized by controlling the amount of polymer binder, also their electrochemical characteristics were measured. The power density of the fabricated ESD-SOFC was 660 mW/cm² power density at 650 °C.

Key Words : Functional surfaces, Deposition process, Superhydrophobic surface, Magnetic composite, Active polymer structure, Solid oxide fuel cell, Electrospray deposition

Student Number: 2009-23907

Contents

Abstract	i
List of figures	vii
Nomenclature	iv
Chapter 1. Introduction	1
Chapter 2. Nano-Thickness Membrane Deposition via Controlled Polymer Interface Fracture	
2-1. Introduction	6
2-2. Experimental	9
2-3. Results and Discussion	12
2-3-1. Mechanism of interfacial fracture in modified PDMS surface	12
2-3-2. Repetitive transfer of the modified PDMS	16
2-3-3. Thickness changes of the transferred patterns followed various process conditions	26
2-3-4. Shape transfer and applications	30
2-4. Summary	34
Chapter 3. Droplet Manipulation on the Magnetic Responsive Superhydrophobic Pillar Arrays	
3-1. Introduction	34
3-2. Experimental	38

3-3. Results and Discussion	42
3-3-1. Preparation of magnetically responsive film	42
3-3-2. Active control of the dynamic structural change of the magnetic pillar arrays by an external magnetic	51
3-3-3. Wetting properties of the magnetically responsive film	55
3-3-4. Remote manipulation of droplets on the magnetically responsive film	61
3-4. Summary	67
 Chapter 4. Fabrication of Solid Oxide Fuel Cell via Electro spray method	
4-1. Introduction	69
4-2. Experimental	73
4-3. Results and Discussion	75
4-3-1. Electro spray deposition process for fabrication of SOFC components	75
4-3-2. LSC cathode deposition by electro spray deposition and electrochemical analysis	77
4-3-3. YSZ electrolyte deposition by electro spray deposition and Structure control via polymer binder	86
4-3-4. ESD Cell fabrication and its electrochemical performances ..	89
4-4. Summary	94
 References	 95
국문 초록	106

List of Figures

- Figure 2-1.** Schematic illustrations for cohesion failure of PDMS block
- Figure 2-2** (a-b) Digital camera images of thin PDMS membranes transferred to aluminum (a) and stainless steel (b).
- Figure 2-3.** (a) The digital camera image of the membrane repetitively transferred to 10 times from same PDMS stamp and its AFM image. Scale bar represents 2 μm . (b) Relative elemental content of C, O, Si of the membrane along depth profile. (c) CA and Height of the membranes repetitively transferred from same PDMS stamp.
- Figure 2-4.** (a) Average roughness of repetitively transferred membranes. Area of AFM image is 10 μm^2 . (b) Contact angle comparison result of PDMS oligomer and membrane transferred glass substrate.
- Figure 2-5.** The FTIR graphs of pristine PDMS and transferred membrane. As shown, major peaks were observed in siloxane chain (1015 ~ 1080 cm^{-1}) and methyl group (796 and 1259 cm^{-1})
- Figure 2-6.** The FTIR spectra results of pristine PDMS, 30s plasma treated PDMS, 1 min plasma treated PDMS and 1 min plasma / heat treated PDMS.
- Figure 2-7.** Simulation result of heat transfer in our membrane transfer process at 20 sec treatment. The temperature of heater is 373.15 K and that of ambient air was 298.15 K.
- Figure 2-8.** Normalized height of transferred patterns as increasing heating time. There were no significant differences with heat annealing time.
- Figure 2-9.** SEM picture of uniform 800-nm line patterns transferred to

silicon substrate. Scale bar represents 2 μm .

Figure 2-10. (a) Representative AFM image of transferred pattern along with its cross-sectional profile. Scale bar represents 2 μm . (b) Change of pattern height with various plasma treatment conditions. (c) Change of pattern height as a function of curing agent to base-agent ratio from 7 % to 20 %. (d) Change of pattern height as a function of curing time from 0.5 and 48 h.

Figure 2-11. (a-c) The SEM images for various transferred patterns: (a) PDMS membrane with holes, (b) PDMS dot arrays, and (c) large concentric circle patterns. Scale bars of (a), (b) and (c) represent 1 μm and 100 μm respectively. (d) A large-area transferred PDMS line patterns on flexible PET film.

Figure 2-12. (a) - (d) Schematics of the protein immobilization and immunoassay. (e) The optical image of the transferred 800 nm nanowell pattern. (f) Fluorescence microscope image of the fluorescein isothiocyanate conjugated goat anti-rabbit IgG. Scale bars of (e) and (f) represents 3 μm .

Figure 3-1. Schematic illustration of pillar fabrication.

Figure 3-2. (a) Magnetic field simulation as distance with magnet. (b)-(c) Height and diameter change by increasing of distance with magnet. (d)-(e) Height and diameter change by number of coating.

Figure 3-3. SEM images of the fabricated magnetically responsive pillars as a function of distance (D) between the magnet and the sample. a. D = 0 mm, b. D = 5 mm, c. D = 10 mm, d. D = 15 mm, e. D = 20 mm, f. D = 25 mm. Scale bars in (a)-(f) are 200 μm .

Figure 3-4. SEM images of the fabricated magnetically responsive pillars as a function of the number of coating-curing processes. (a)-(c) are samples without CNP coating and (d)-(f) are samples with CNP coating. Scale bars in (a)-(f) are 200 μm .

Figure 3-5. SEM images of the magnetically responsive pillar arrays prepared using different amount of sprayed mixture comprising

of precured polymers and magnetic particles. 0.5 ml, 1.0 ml and 1.5 ml solutions were used for the resulting samples in (a), (b), and (c), respectively.

Figure 3-6. (a) Simulation of magnetic flux density around the pillar array when a magnet is placed under the sample. (b) Side views of the dynamic response of the pillar array when the magnet approaches the targeted pillars (red arrows in Fig. 3a) at a horizontal distance “d” from the edge of the magnet. Scale bars are 200 μm . (c) Top-views of the magnetically responsive pillar array placed on a rectangular magnet. The pillars located directly above the magnet are significantly bent. The region of bent pillars rotates along with the magnet. Scale bars are 1 cm.

Figure 3-7. Top-views of the magnetically responsive pillar arrays (a) with and (b) without applied magnetic field.

Figure 3-8. (a) SEM images of a pillar without (left) and with (right) CNP coating. (b) Contact angles of DI water on various magnetically responsive pillar arrays with different numbers of coating-curing processes when no magnetic field is applied to the sample. (c) Contact angles of DI water on various magnetically responsive pillar arrays with different numbers of coating-curing processes when the pillar arrays are fully flattened on the substrate by an applied magnetic field. (d) Roll-off angles of DI water on various magnetically responsive pillar arrays for different numbers of coating-curing processes and magnetic field application. The symbol “(c)” on the x-axis of the graphs in (b)-(d) represents CNP coated samples.

Figure 3-9. Schematic illustration of droplet wetting on various magnetically responsive pillar arrays related to the CNP coating and the number of coating-curing processes when no magnetic field is applied to the samples.

Figure 3-10. Schematic illustration of droplet wetting on various magnetically responsive pillar arrays related to the CNP coating and the number of coating-curing processes when the pillar arrays are bent by an applied magnetic field.

Figure 3-11. Roll-off angles of DI water with two different droplet volumes on various magnetically responsive pillar arrays for different numbers of coating-curing processes and magnetic field application. The symbol “(c)” on the x-axis of the graphs in (a)-(b) represents CNP coated samples.

Figure 3-12. (a) Schematic illustration of active droplet manipulation on the magnetically actuating hierarchical pillar array. When the pillars are bent by a magnetic force, a local difference in the potential energy (“PE”) is generated in the array. Furthermore, actuation of the pillars provides a driving force (kinetic energy, “KE”) for the droplet to move along the direction of the pillars. As a result, the droplet moves towards the location of the bent pillars. (b) Demonstration of continuous manipulation of the droplet on the magnetically responsive film with a neodymium magnet.

Figure 3-13. Applications of the magnetically responsive film with superhydrophobic wetting properties. (a) Demonstration of precise manipulation of droplets to specific targeted locations. A blue coloured droplet is manipulated with a permanent neodymium magnet to the right until it contacts the yellow droplet. After contacting the yellow droplet, the two droplets merge together, generating a larger green droplet. The merged droplet is further transported using the magnet to the red droplet, forming another merged droplet. (b) Guided rolling-off of the droplet to targeted locations. Pillar arrays on a magnet are flattened on the substrate along the magnetic field direction, forming an open channel on the surface. As a result, a droplet can be rolled off towards a specific target location along the channel. The channel direction can be easily tuned by rotating the magnet. (c) Demonstration of anti-icing properties of the film. Because of the superhydrophobic wetting properties, ice particles form with nearly perfect spherical shapes on the film. These ice particles can be removed from the surface simply by actuating the pillar arrays with a magnet.

Figure 4-1. Graphical presentation of the SOFC structure.

Figure 4-2. Schematic illustration for ESD process

- Figure 4-3.** Planar (a)-(c) and Sectional (d)-(f) SEM images of the LSC cathode layer fabricated by ESD process under different weight ratio between LSC and PVP to solvent : (a) and (d) 10 : 5 (b) and (e) 10 : 10 (c) and (f) 10 : 20. Scale bars represent 2 μm in (a)-(c) and 1 μm in (d)-(f).
- Figure 4-4.** Electrochemical performances of LSC fabricated by ESD process with different PVP amount at 650 $^{\circ}\text{C}$. (a) LSC : PVP = 10 : 5 (b) LSC : PVP = 10 : 10 (c) LSC : PVP = 10 : 20.
- Figure 4-5.** Impedance spectra results of LSC fabricated by ESD process with different PVP amount. All the impedance spectra was measured at OCV condition and 650 $^{\circ}\text{C}$ (a) LSC : PVP = 10 : 5 (b) LSC : PVP = 10 : 10 (c) LSC : PVP = 10 : 20.
- Figure 4-6.** SEM images of deposited LSC by ESD process with different solvent conditions (a) Ethanol : DI water = 7 : 3 (b) Only ethanol.
- Figure 4-7.** Electrochemical performances of LSC fabricated by ESD process. (a) Ethanol : DI water = 7 : 3 (b) Only ethanol.
- Figure 4-8.** Impedance spectra of LSC fabricated by ESD process at 650 $^{\circ}\text{C}$. (a) Ethanol : DI water = 7 : 3 (b) Only ethanol.
- Figure 4-9.** SEM images of YSZ layer deposited with different YSZ/PVB ratio: (a) 7 wt%/ 2 wt% (b) 4 wt% / 2 wt% (c) 2 wt%/2 wt%, scale bars represent 2 μm .
- Figure 4-10.** Cross-sectional SEM images of ESD cell. (a) 4 μm and (b) 2 μm thickness of YSZ. Scale bars represent 2 μm .
- Figure 4-11.** Electrochemical performances of cells fabricated by ESD process. 2 μm (a) and 4 μm (b) thickness of YSZ.
- Figure 4-12.** Impedance spectra results of the ESD cells fabricated by ESD process. 2 μm (a) and 4 μm (b) thickness of YSZ.

Nomenclature

R_a	Average roughness
ρ	Density
C	Heat capacity
k	Thermal conductivity
θ_c	Theoretical static contact angle
θ_w	Equilibrium contact angle
j	time index ($1 \leq j \leq m$)
f	Area fraction of the solid surface
γ_{lv}	Surface energy of liquid
θ_r	Receding contact angle
θ_a	Advancing contact angle
R_Ω	Area specific ohmic resistance
R_p	Area specific polarization resistance

Chapter 1. Introduction

During the last several decades, many kinds of surfaces which have specific functions such as dry adhesive, self-cleaning, and energy conversion have been found from nature.[1-3] Those structures have been adapted and optimized to the environment over the centuries by maximizing their functions. Inspired from those structures, many researches to fabricate such functional surfaces have been conducted. Accordingly, micro/nano-scale fabrication technology for manufacturing functional surfaces and its applications have been under the remarkable development. Especially, surface deposition methods such as dip coating, spin coating, sputter, CVD, PVD and ALD are widely used to make functional surfaces and further modify surface properties.[2-7] Through the deposition methods, not only the chemical properties but mechanical characteristics can be changed.

One of the most commonly used functional surface is hydrophobic structures. Main ways for making hydrophobic surfaces are coating another material with low surface energy and fabricating micro/nano-scale roughness. Various materials have been used as low surface energy materials, polytetrafluoroethylene (PTFE), polypropylene (PP), octafluorocyclobutane (C_4F_8), carbon nanotube (CNT) and also the thin film and patterns of those materials can be deposited via spin

coating,[8] RF plasma,[9] CVD,[10] and PLD.[11]

Meanwhile, the deposition methods are substantially important for the energy devices. Above all, at the ceramic particle based fuel cell, various deposition methods based on powder process and the vacuum process have been developed to fabricate dense electrolyte and porous cathode structures.[11-15] Since the interface and micro structures of the surfaces which have relations with resistance and reaction site are influenced by fabrication methods, uniform and facile processes are required for high-performance fuel cell.

With the development of new technology, interests in the fabrication of more complex and improved functional surfaces have increased. But listed conventional methods have some difficulties in making structural functional surfaces. For example, the chemical coating can be used to modify properties of surfaces but it is hard to make complex structures. Meanwhile, deposition methods based on the semiconductor process need particular conditions such as vacuum, gas condition and high temperature. As well, slow process speed and preparation of target material can be disadvantages of the conventional deposition processes. Accordingly, demands for a novel deposition method to address the limitation of the conventional methods have been raised.

In the thesis, we suggest novel deposition processes to fabricate and control multiscale functional structures. Elastic polymers play an important role as transferred patterns, composite bodies and binders of ceramic particles in each

fabrication process: polydimethyl siloxane(PDMS) can be transferred as thin film or support magnetic composite pillar. Additionally, polyvinyl butyral(PVB) and polyvinyl pyrrolidone(PVP) assist adhesion and mass transportation of the ceramic particles after the deposition process. Those methods can fabricate micro/nano structures with many advantages, for example, mold-free and fast fabrication as well as uniform patterning. The results show that the patterns can be used to wettability control and energy conversion at the surfaces.

In chapter 2, we report that a thin layer of polydimethyl siloxane (PDMS) in the thickness range of 66 to 78 nm can be generated multiple times (> 10) by utilizing irreversible bonding with oxygen plasma treatment and controlled interfacial fracture. The clean cleavage is attributed to the built-in stress at the fracture interface during the plasma treatment, resulting in the repetitive formation of a smooth membrane of ~ 5 nm roughness from the bulk PDMS. And then, we control the height of transferred patterns via oxygen plasma treatment conditions and intrinsic characteristics of PDMS stamp. The method can be used to transfer various micro- and nanopatterns without a residual layer as well as to form nanogrooves of controlled dimension. Also, we achieved highly specific protein immobilization on the patterned surface of a solid substrate in a site-directed manner.

In chapter 3, we investigate the magnetic responsive and superhydrophobic

pillar array via the spray method. The magnetic pillars grow in the magnetic field direction during the spray process, and represent enormous deflection under the magnetic force. We analyzed structure changes and wetting characteristics of the pillars as varying the strength of magnetic field and the number of coatings. The size of pillars increases with repeated coating process, which make the pillars more hydrophobic. Furthermore, dual-roughness of pillars dramatically decreases its CA hysteresis. The large bending of the pillars generates geometrical potentials, decreasing the droplet ROAs on the structures. Using the active property of magnetic pillar, we adjust the sliding direction of the droplet by the orientation of the magnet and, additionally, we show active droplet manipulation and mixing result on the pillar structure via only structural modulation.

In chapter 4, we present a fabrication process to make the components of the solid oxide fuel cell (SOFC) using the electrospray deposition (ESD) method which can deposit a uniform membrane through simple steps and further evaluate its performances. The components of the SOFC such as anode functional layer (AFL), electrolyte layer, cathode functional layer (CFL) and cathode layer could be fabricated by the ESD method followed by the annealing process. Especially, we could get dense membrane from deposited ceramic powder connected with binding polymer. During the annealing process, the morphology of the membrane is determined by the amount of the binder. Under the low concentration of the

binding polymer, the porous membrane is fabricated, but under the high concentration, dense membrane morphology is attained. As a result, we could adjust the morphology of the ceramic membrane via the ESD method and optimize the structure of SOFC components. Using the ESD process, we fabricate two cases of the SOCF: 1.ESD cathode combined conventional process case and 2.ESD cathode/electrolyte deposited on the anode substrate. Also their electrochemical performances are measured.

Chapter 2. Nano-Thickness Membrane Deposition via Controlled Polymer Interface Fracture

2-1. Introduction

Elastic and deformable materials are used widely in applications including micro/nano fabrication and functional structures. A broad range of physical and chemical properties, including the elastic modulus, strength, optical properties and surface characteristics, can be controlled and adapted to specific purposes by varying the curing conditions and chemical composition, complex mixture and physical treatment (i.e., UV radiation and plasma treatment). Furthermore, rubber-like materials can be used as compliant substrates to form bilayer structures with a rigid film by depositing additional layers or chemically modifying surfaces.

A thin membrane of an elastic material has a number of advantages, including flexibility, transparency, permeability and the ability to make conformal contact with other materials. There have been a number of reports of the fabrication of mechanically robust and functional thin membranes using spin coating, spray coating, and electrochemical synthesis, and such ultrathin membranes have applications as gas barriers, chemical sensors and in selective extraction of the metal ions.[16] In addition, fabrication of advanced membranes via micro/nano

patterning or designing composite structure may be feasible.

In this article, we describe a simple and reproducible method of preparing thin membranes that can be repeatedly separated from pristine polydimethyl siloxane (PDMS), with a uniform thickness of 60 to 80 nm. By exploiting tight bonding, combined with heating and oxygen plasma treatment, subsequent cleavage via controlled interfacial fracture can be achieved. When PDMS was treated with a plasma or ultraviolet (UV)-generated ozone. Since the modified layer has a large built-in stress and mechanical and chemical properties different from those of pristine bulk PDMS,[17, 18] failure can occur during a contact-based transfer process. In this way, various micro-/nanoscale patterns can be generated on receiver substrates including glass, silicon dioxide (SiO₂) and flexible polymers. A number of modified decal transfer lithography (DTL) methods, based on annealing- or solvent swelling-induced cohesive mechanical failure (CMF) processes, have been reported.[19-23]

The process described here could be repeated more than ten times without appreciable variation in properties of the transferred layers. As we shall show, varying the experimental conditions allows us to control the location of the fracture plane, and hence the thickness of the transferred layer. The surface oxidation could be controlled by varying the treatment time and plasma power, and was affected by the crosslinking density, which could be modified in a number of ways, including by changing the amount of curing agent, the baking

time and the temperature.[24-27] The thickness of transferred membrane could be controlled by varying the process conditions, because the location of the interfacial failure plane depends on the plasma treatment conditions and the crosslinking density in the PDMS. Various micro- and nanostructures could be fabricated without a residual layer by combining controlled interfacial fracture and pattern transfer methods. Because the substrate and transferred layer have different wettabilities, we were able to demonstrate the use of well-defined protein arrays for immunoassay applications.

2-2. Experimental

2-2-1. Fabrication of PDMS stamp

The silicon masters having line pattern were prepared by conventional photolithography and etching processes. The line pattern had 800 nm width with equal spacing. Its height was 600 nm and the patterned field was 3 by 3 cm. To prepare PDMS replicas, the base and curing agent of Sylgard 184 (Dow corning) were mixed at 10:1 wt% fraction, poured onto the silicon masters and cured at 70 °C for various baking times (0.5 ~ 48 h). Then the cured PDMS stamps were peeled from the silicon masters and cut prior to use.

2-2-2. Repetitive transfer by interfacial fracture

The prepared PDMS stamp and substrates (bare silicon wafer, glass, or PET film) were treated by oxygen plasma under various conditions (200 mTorr, 7 ~ 18 W) for the duration of 30 s to 1 min. Then, the stamp was uniformly placed on the substrate, and then heated on a hot plate for 20 s at 100 °C. Subsequently the stamp was peeled off from the substrate, leaving behind a thin PDMS layer on the receiver substrate. Especially, The PET film was spin coated with Adhesion primer (Minuta technology, KOREA).

2-2-3. Atomic force microscopy (AFM) and scanning electron microscopy (SEM)

The heights of transferred membranes and patterns were measured by AFM (XE-150, PSIA) via non-contact mode (NCHR probe, radius of curvature < 10 nm) with the scan rate of 0.5 Hz, and SEM (S-48000, Hitachi, Japan) with a Pt layer of 30 nm thickness to avoid charging effect. The emitted energy was 10 kV with 1 nm resolution.

2-2-4. Auger Electron Spectroscopy (AES) and Fourier Transform Infrared (FTIR) Spectrophotometer

The elemental contents of a transferred membrane of ~80 nm thickness were analyzed with AES (PHI-660, Perkin-Elmer) to measure depth profiles of three major elements (C, O, Si). FTIR Spectrophotometer results were recorded on a Nicolet 6700, in the mid range from 4000 to 600 cm^{-1} with 1 cm^{-1} resolution at room temperature (about $22 \pm 1^\circ\text{C}$). Both pristine PDMS membrane and transferred membrane were measured in absorbance mode, and the Ge crystal was used to measure thin layer (< 300 nm) in the FTIR analysis.

2-2-5. Protein Immobilization and Immunostaining

For protein immobilization, human fibronectin (HFN) was used as a representative protein. Prepared samples were covered with HFN solution (5 $\mu\text{g/ml}$, Sigma) and incubated for 30 min at room temperature. After immobilization process, samples were washed with PBST (0.1 % Triton X-100 (Sigma) in PBS solution) for three times to remove unbound HFN and treated with blocking solution (2 % bovine serum albumin (BSA, Sigma) in PBST) for 30 min to reduce non-specific binding of antibodies. Rabbit anti-fibronectin antibody solution (1:250 in blocking solution, Sigma), primary antibody solution, was pipetted onto fibronectin-immobilized samples and incubated for 1 h at room temperature. After washing with PBST for three times, fluorescein isothiocyanate (FITC) conjugated goat anti-rabbit IgG (1:250 in blocking solution, Sigma), secondary antibody solution, was pipetted onto samples, incubated for 1 h at room temperature in darkness and washed for three times with PBST. To prevent photobleaching of the dye, samples were coated with ProLong Gold antifade reagent (Invitrogen) and observed with fluorescence microscopy (Eclipse Ti, Nikon).

2-3. Results and Discussion

2-3-1. Mechanism of interfacial fracture in modified PDMS surface

We were able to achieve repeatability of the location of the failure plane at the interface of the plasma treated layer and the bulk pristine PDMS, which results in a clean interface between the layers, and a controlled thickness of the transferred membrane. In the presence of an external force, or residual stress, fracture typically occurs at the interface of a bilayer system due to the large mismatch in elasticity, so that cleavage is initiated due to a spatial gradient of the stress.[28] Because of this mismatch in the elasticity, CMF can be exploited to create micro and nanostructures.[29] When a peeling force is applied to the bilayer system, the peeling stress is concentrated at the interface due to the mismatch in the mechanical properties of the materials.[28]

The experimental procedure is illustrated in Figure 2-1. A bulk PDMS block and a receiver substrate (silicon, glass, or PET film) were subjected to oxygen plasma treatment, and then placed in direct contact, followed by a short period of heat treatment (20 s at 100°C). Following removal of the PDMS block, a thin silica-like oxidized layer was transferred to the substrate. The thickness of this layer was in the range 60 - 80 nm. It is well known that oxygen plasma treatment can introduce hydrophilic silanol (-OH) groups onto the surfaces such as silicon,

glass, and polymers.[30] These polar groups lead to an irreversible seal by dehydration via the following chemical reaction: $\text{SiOH} + \text{SiOH} \rightarrow \text{Si-O-Si} + \text{H}_2\text{O}$. [31] The modified PDMS surface was much stiffer than the bulk PDMS, and had a lower thermal expansion coefficient due to the significant insertion of oxygen networks (i.e., siloxane bonds). The penetration depth of siloxane bonds is typically ~80 nm following oxygen plasma treatment,[32] and the elastic modulus of the modified skin layer was 3–4 orders of magnitude larger than that of bulk PDMS.[33, 34] This large mismatch in elasticity, in combination with the irreversibly bonding at the surface, results in cohesion failure during peeling. The combined process of heating and peeling was able to induce clean cleavage of the oxidized PDMS layer onto various substrates, including silicon, aluminum, stainless steel, and polymer (see Figure 2-2).

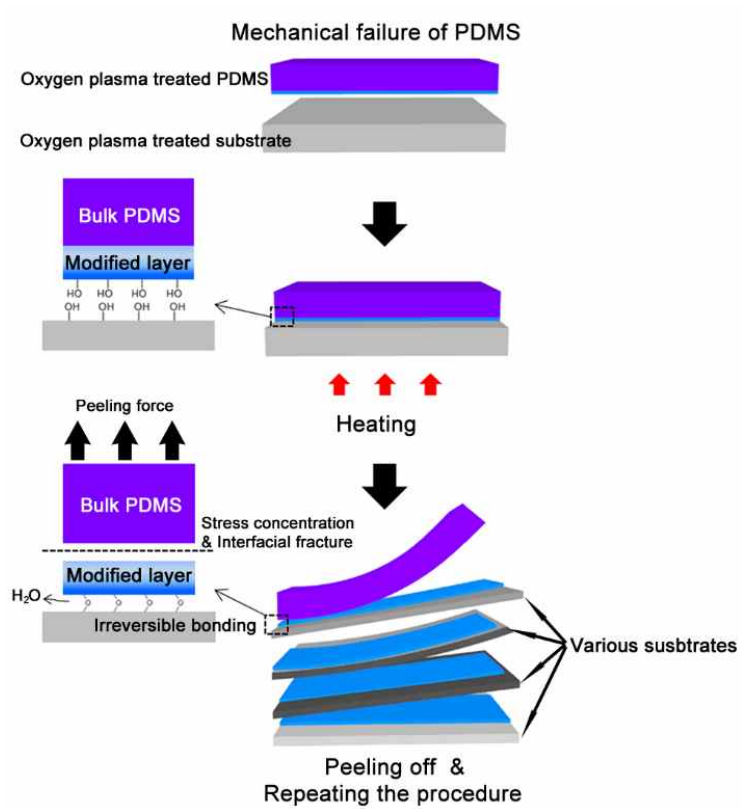


Figure 2-1. Schematic illustrations for cohesion failure of PDMS block

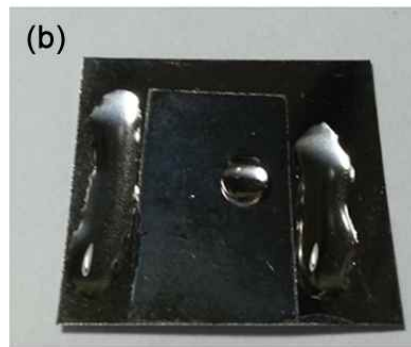
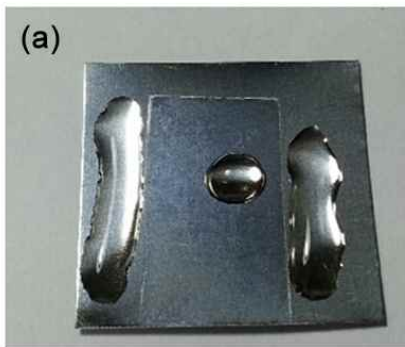


Figure 2-2. (a-b) Digital camera images of thin PDMS membranes transferred to aluminum (a) and stainless steel (b).

2-3-2. Repetitive transfer of the modified PDMS membrane

We were able to transfer the modified PDMS membranes from the same PDMS block onto 4-inch silicon wafers more than ten times. Furthermore, uniform properties of the transferred layer were achieved, as shown in Figure 2-3a. The transferred region was hydrophobic with a contact angle (CA) for water of 110° , whereas the silicon wafer exhibited a CA of 20° . The CA was similar to that of the pristine PDMS, suggesting that the transferred membrane exhibited a silica-like skin layer, and an unmodified PDMS layer at the fracture surface. Depth profiles of the C, O, and Si fraction based on Auger electron spectroscopy (AES) measurement are shown in Figure 2-3b.: the element composition was approximately 40% C, 30% O, and 30% Si, at the fracture interface, and this composition was maintained for approximately 50 nm into the thin layer. This composition deviates slightly from that of the bulk PDMS (50% C, 25% O, and 25% Si). At greater depths into the sample there was a sharp increase in the oxygen concentration ($\sim 50\%$) at 10 nm from the bottom surface (i.e., the surface that was exposed to the plasma), which is consistent with previous measurements of the surface following similar oxygen plasma treatment.[32] Figure 2-3c shows that the thickness and CA of the membrane was consistent for more than ten transfer steps. The AFM image shown in Figure 2-4a indicates that the surface was relatively clean and smooth, with an average roughness of $R_a < 6$ nm, even

after repeated transfers. In contrast to the PDMS oligomer, the transferred membranes exhibited constant hydrophobicity following washing with acetone, as shown in Figure 2-3b. Moreover, the properties of the siloxane chain and methyl group observed using Fourier transform infrared (FTIR) spectroscopy (see Figure 2-5) suggest that the membrane can be expected to be hydrophobic.

Figure 2-6 shows FTIR spectra of pristine PDMS, plasma treated PDMS, and heat and plasma treated PDMS. The most marked variation was $1018 - 1080 \text{ cm}^{-1}$, corresponds to the Si-O-Si chain, the peak at 1259 cm^{-1} , which corresponds to the symmetric methyl deformation of Si-CH₃, and the peak at 796 cm^{-1} , which corresponds in-plane rocking vibration in Si-CH₃. [35, 36]

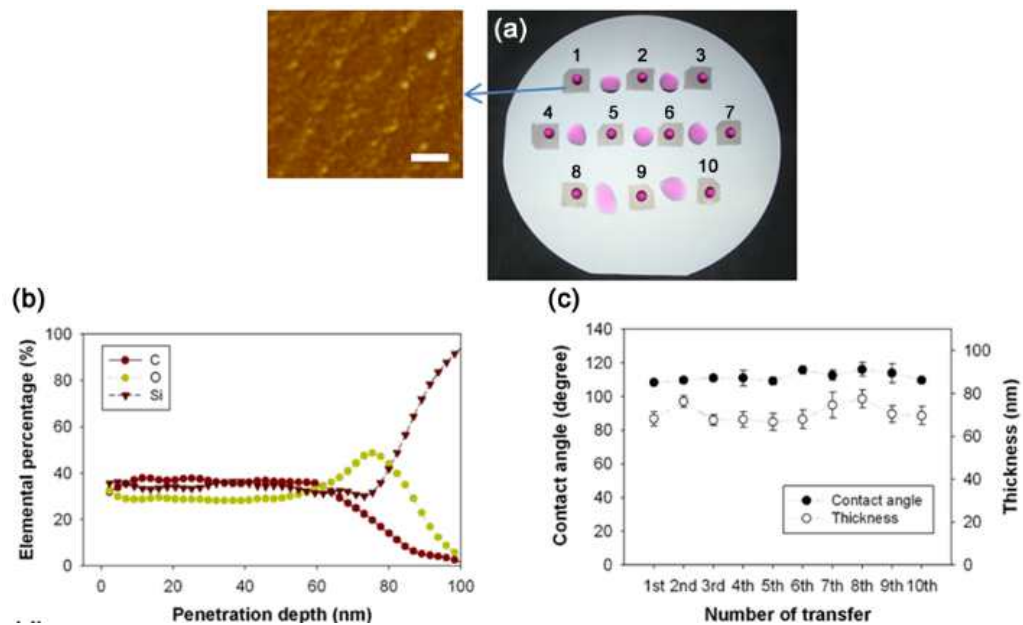


Figure 2-3. (a) The digital camera image of the membrane repetitively transferred to 10 times from same PDMS stamp and its AFM image. Scale bar represents 2 μm . (b) Relative elemental content of C, O, Si of the membrane along depth profile. (c) CA and Height of the membranes repetitively transferred from same PDMS stamp.

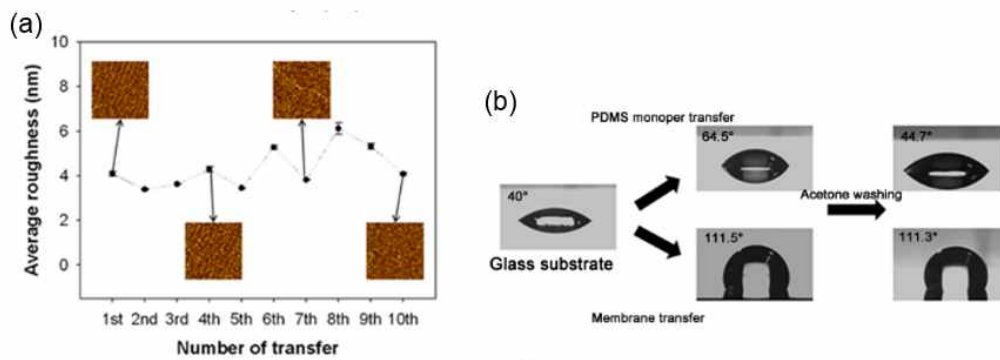


Figure 2-4. (a) Average roughness of repetitively transferred membranes. Area of AFM image is $10 \mu\text{m}^2$. (b) Contact angle comparison result of PDMS oligomer and membrane transferred glass substrate.

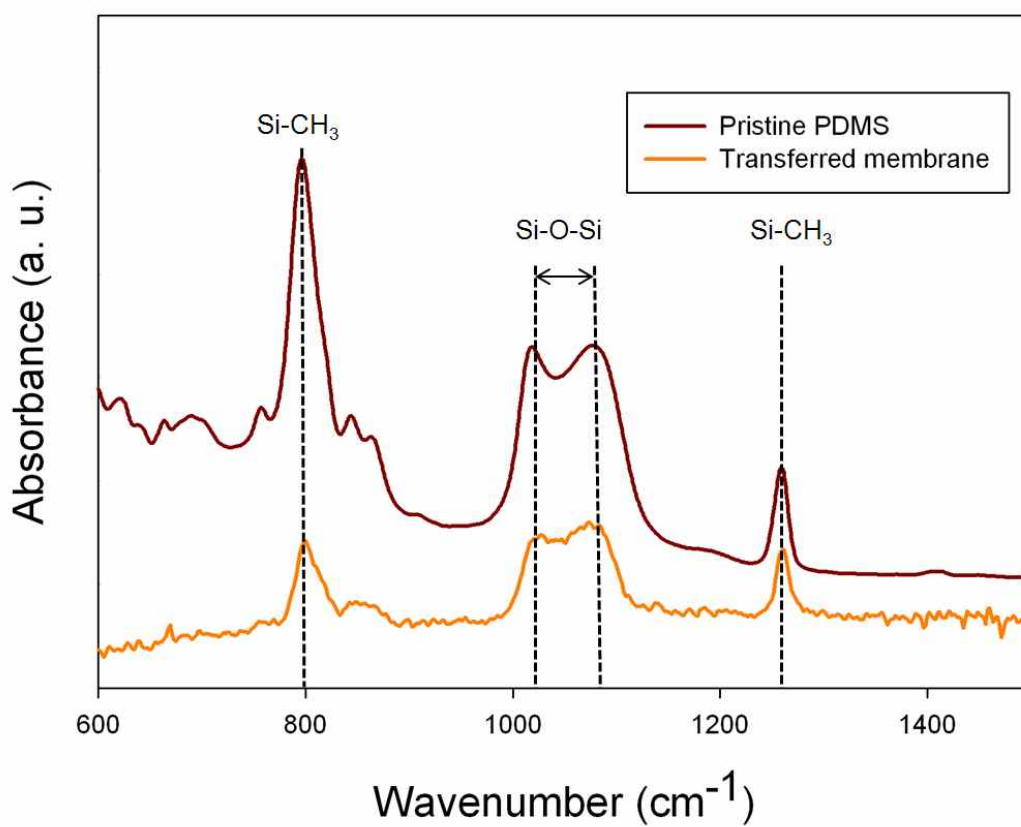


Figure 2-5. The FTIR graphs of pristine PDMS and transferred membrane. As shown, major peaks were observed in siloxane chain ($1015 \sim 1080 \text{ cm}^{-1}$) and methyl group (796 and 1259 cm^{-1})

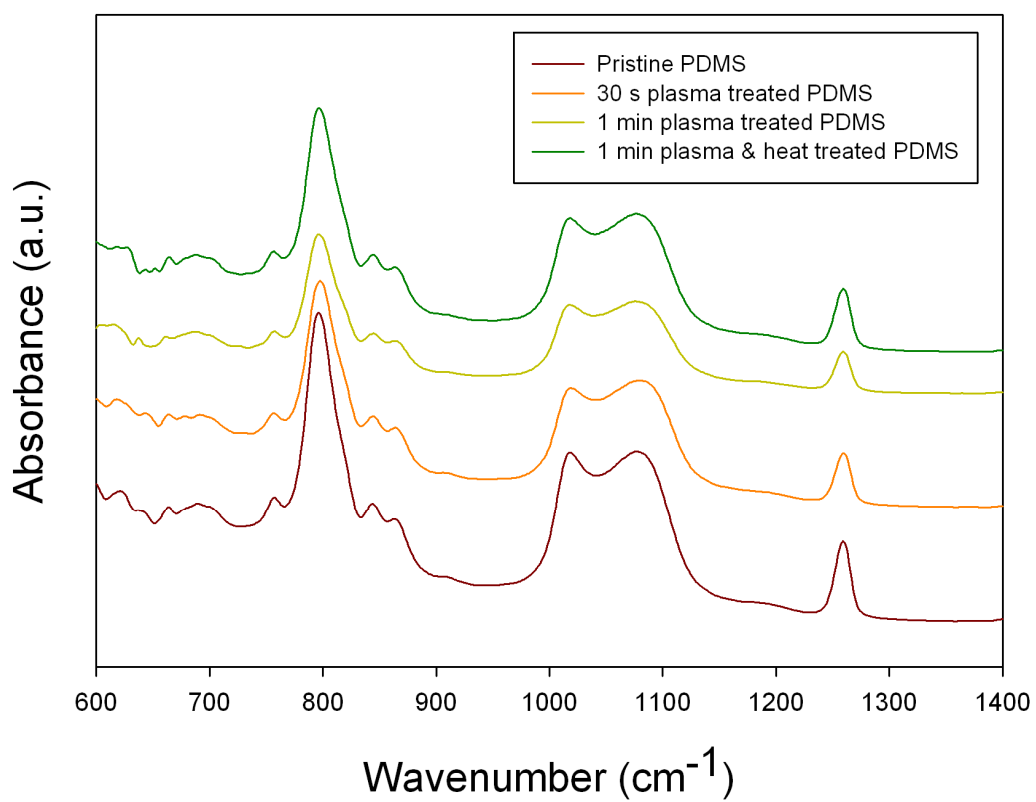


Figure 2-6. The FTIR spectra results of pristine PDMS, 30s plasma treated PDMS, 1 min plasma treated PDMS and 1 min plasma / heat treated PDMS.

Following plasma treatment, the chemical composition of the surface of the PDMS was converted to a silica-like (SiO_x) formation. The peaks at 1018–1080 cm^{-1} decreased in intensity because the number of asymmetric Si-O-Si bonds decreased.[37] The loss of methyl functional groups is consistent with the decrease in the intensity of the peaks at 1259 cm^{-1} . Following heat treatment, the intensity of the peak at 1018–1080 cm^{-1} corresponding to Si-O-Si bonds increased again, which is attributable to condensation of the unstable plasma-treated region.[38, 39] This reaction transforms the plasma-treated layer into well-defined thin membrane, which has different mechanical properties to that of the bulk PDMS, which enables repeatable membrane transfer.

The results of simulations (see Figure 2-7) show that the temperature profile extends for a few hundreds of micrometers into the bulk. The commercial software COMSOL Multiphysics was employed to simulate the heat transfer in our process. The heat transfer was modeled with transient convection-conduction equation as

$$\rho C \left(\frac{\partial T}{\partial t} + \mathbf{u} \nabla \cdot \mathbf{T} \right) = \nabla \cdot (k \nabla T)$$

where ρ (kg/m^3), C ($\text{J/kg}\cdot\text{K}$) and k ($\text{W/m}\cdot\text{K}$) denote the density, heat capacity and thermal conductivity respectively. We used COMSOL material library for value of Si and the ρ , C and k of PDMS (Sylgard 184) were 0.15, 0.97 and 1460

from datasheet of Dowcorning. It follows that although heat penetrates much deeper than the chemical modifications due to the plasma treatment, significant effects occurs only in the regions that have been affected by both the thermal and plasma treatment processes. Further evidence for this is that there was no significant change in the thickness of the membrane as function of the heating time (Figure 2-8). It follows that control over the thickness of the membranes can be achieved by varying the conditions in plasma process.

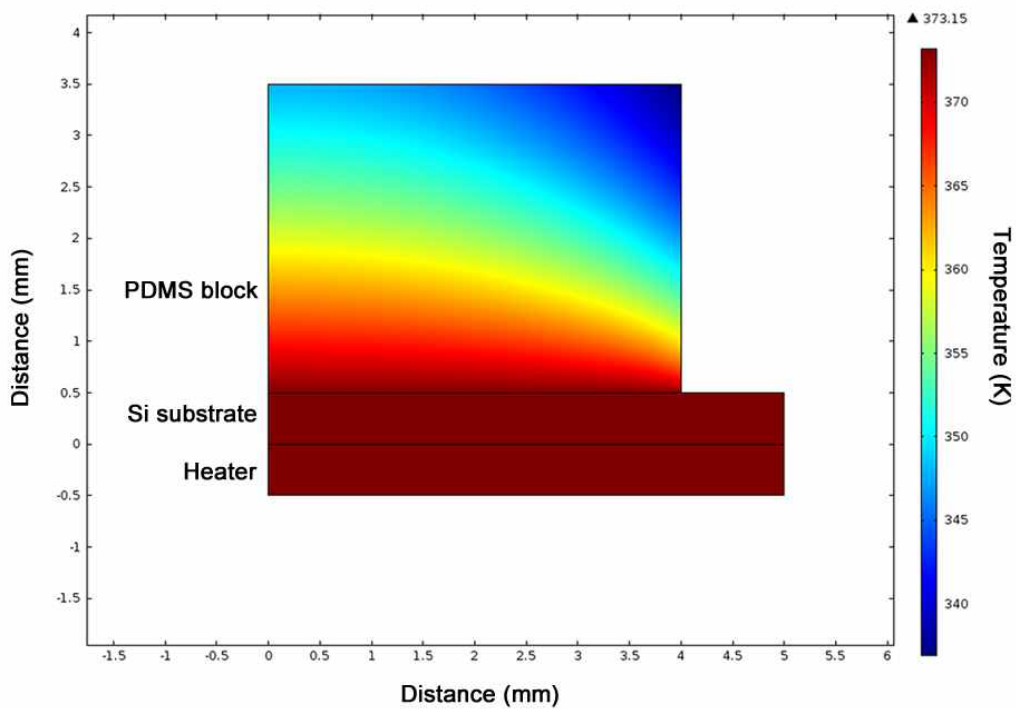


Figure 2-7. Simulation result of heat transfer in our membrane transfer process at 20 sec treatment. The temperature of heater is 373.15 K and that of ambient air was 298.15 K.

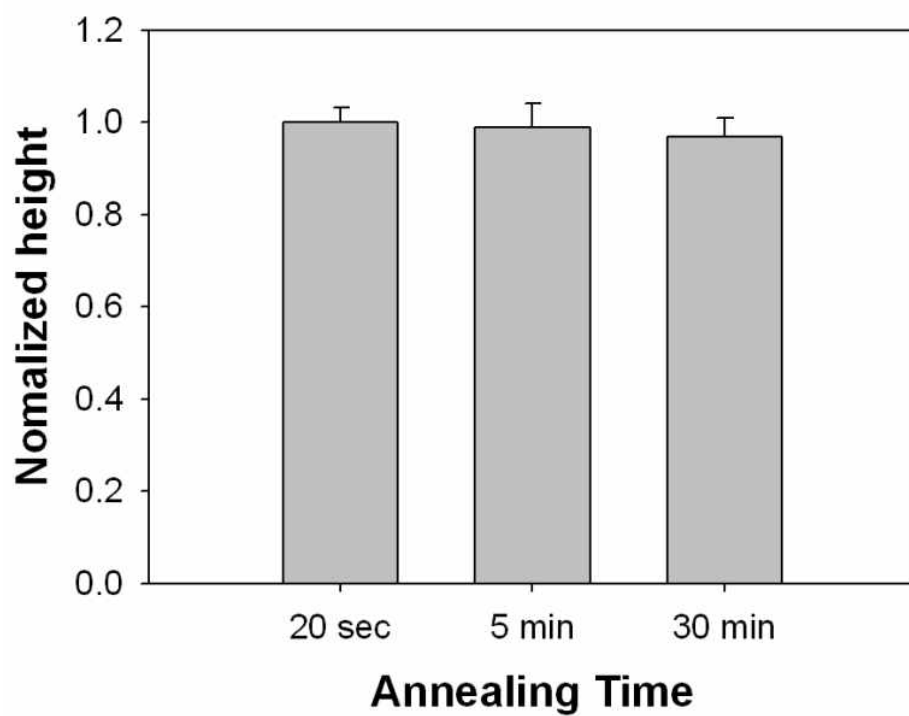


Figure 2-8. Normalized height of transferred patterns as increasing heating time.

There were no significant differences with heat annealing time.

2-3-3. Thickness of the transferred patterns followed various conditions

As To determine the role of the oxygen plasma, we first investigated the thickness of oxidized layer using an 800 nm pitch line-and-space pattern with the height of 600 nm (see Figure 2-9). It is well-known that the oxygen diffusivity and plasma density affect the thickness of the modified region of PDMS;^[40] therefore, the location of the cohesion failure are expected to be determined by the penetration depth of the plasma treatment. Figure 2-10a shows an atomic force microscope (AFM) image of a representative PDMS pattern following the pattern transfer process, demonstrating that the patterned surface was uniform over the large area, with a rounded surface profile. The height of the patterned features was in the ranged 125–330 nm, which is greater than that of the uniform membrane shown in Figure 2-3: this is attributed to enhanced oxidation via lateral diffusion of oxygen.

The thickness of transferred line patterns depended on the plasma treatment conditions, i.e., the plasma power and exposure time. Figure 2-10b shows the results of pattern transfer with different plasma treatment conditions. The samples were cured for 1.5 h with a mixing ratio of 10:1. The average thickness of the patterns treated with a power of 18 W of power for 1 min was ~340 nm. When a smaller power (7 W) was used, the average thickness reduced to ~ 230 nm, and when a shorter exposure time (30 s) was used, the average height was ~220 nm.

In addition to the plasma treatment conditions, we were able to control the thickness of the oxidized layer by varying the diffusivity of oxygen plasma. The free volume of the polymers, which is related to the crosslinking density, affects the oxygen diffusivity, as well as the mechanical properties such as modulus,[25] storage of uncured molecules,[41] and permeability.[42] In addition, the curing conditions during crosslinking can modify these characteristics.[43] Hence, the depth of the PDMS skin layer could be controlled by varying the ratio of the curing agent to the base polymer, as shown at Figure 2-10c, in which the amount of curing agent was varied in the range 7 % ~ 20 %, indicating that the apparent oxygen diffusivity in the harder PDMS was less than that in the softer PDMS. It appears that, under the current conditions, the penetration depth of the plasma was approximately equal to equivalent to the height of transferred pattern, which was in the range 160–340 nm.

Similarly, the variation in the thickness of the transferred patterns is shown in Figure 2-10d as a function of the curing time (with fixed curing conditions and a mixing ratio of 10: 1). A curing of 20 min resulted in a thickness of ~330 nm, which was decreased to ~125 nm following curing 6 h. As the curing time increased further, the pattern thickness saturated at ~120 nm. Such saturation is consistent with the previous report by Schiabone et al.,[26] suggesting that the modulus is correlated with the thickness of transferred pattern.

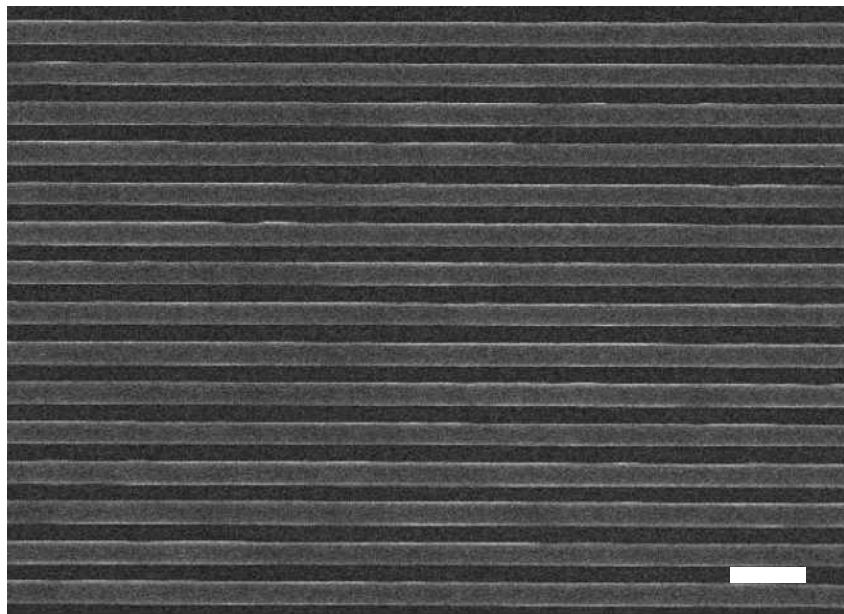


Figure 2-9. SEM picture of uniform 800-nm line patterns transferred to silicon substrate. Scale bar represents 2 μm .

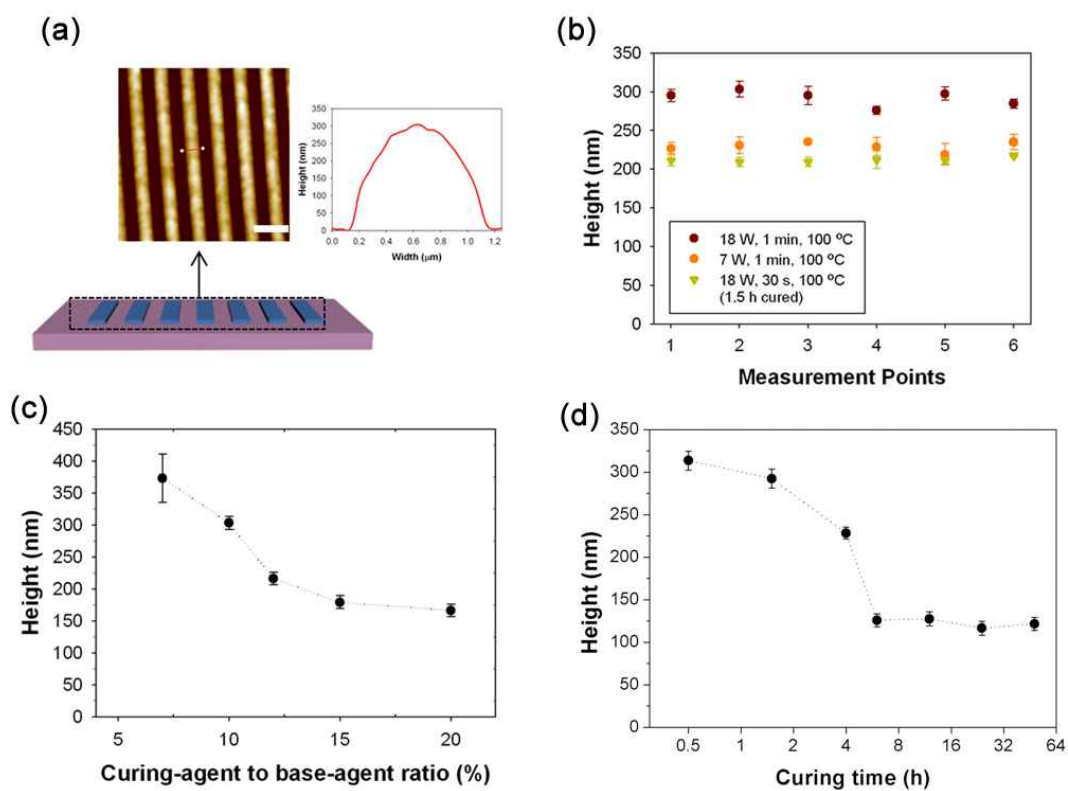


Figure 2-10. (a) Representative AFM image of transferred pattern along with its cross-sectional profile. Scale bar represents 2 μm . (b) Change of pattern height with various plasma treatment conditions. (c) Change of pattern height as a function of curing agent to base-agent ratio from 7 % to 20 %. (d) Change of pattern height as a function of curing time from 0.5 and 48 h.

2-3-4. Shape transfer and applications

Figure 2-11 shows that various patterns can be formed on rigid and flexible substrates, including polyethylene terephthalate (PET), with same process parameters. By the coating of the surface with an adhesive primer that contains silane compounds, silanol groups can be formed following the oxygen plasma treatment. This surface treatment facilitates pattern transfer onto a flexible substrate.

One of the most important advantages of this approach is its generation of a residue-free pattern. Because the transferred pattern is hydrophobic, but the exposed silica surface was very hydrophilic, it is possible to create protein array that were aligned to a tolerance of 800 nm. Figure 2-12 shows the wells patterned on the SiO₂ substrate. In general, proteins have higher affinity for polar surfaces, such as SiO₂, than non-polar surface; thus proteins can be selectively immobilized on the exposed SiO₂ regions. [44, 45]

Although there exist a number of methods to create protein arrays, including nanoimprint,[46] photo lithography,[47] and dip-pen lithography,[48] these methods are typically relatively expensive and require multiple process steps. Using the membrane transfer method described here, we fabricated sub-micron well structures on a glass substrate. The patterned substrate was covered with HFN solution at room temperature to achieve protein immobilization, and

subsequently visualized through the specific antibody-antigen reaction between rabbit anti-fibronectin and fluorescein isothiocyanate (FITC) conjugated goat anti-rabbit IgG. Figure 2-12f shows fluorescence image, revealing well-aligned protein arrays.

The transferred patterns act as a physically deposited hydrophobic self-assembled monolayer and do not require a mask or lift-off process. The process is therefore, not only facile and low-cost but also biocompatible, and hence has potential applications in biosensors and observation of protein-cell interactions.

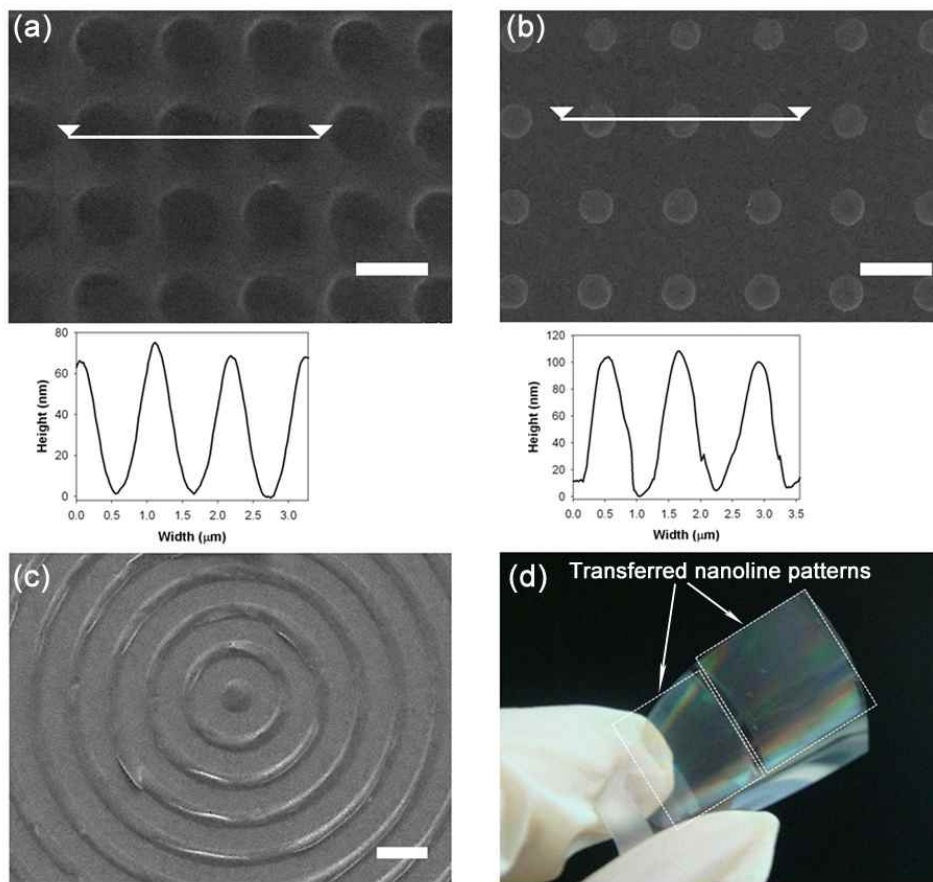


Figure 2-11. (a-c) The SEM images for various transferred patterns: (a) PDMS membrane with holes, (b) PDMS dot arrays, and (c) large concentric circle patterns. Scale bars of (a), (b) and (c) represent 1 μm and 100 μm respectively. (d) A large-area transferred PDMS line patterns on flexible PET film.

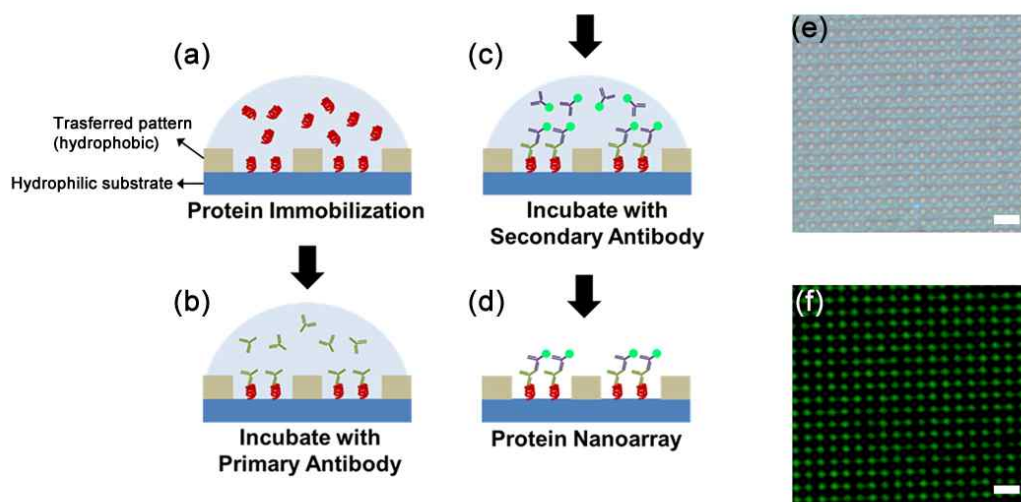


Figure 2-12. (a) - (d) Schematics of the protein immobilization and immunoassay. (e) The optical image of the transferred 800 nm nanowell pattern. (f) Fluorescence microscope image of the fluorescein isothiocyanate conjugated goat anti-rabbit IgG. Scale bars of (e) and (f) represents 3 μm .

2-4. Summary

We have demonstrated controlled and repetitive transfer of thin PDMS membranes via CMF from bulk PDMS block on substrates including SiO₂ via oxygen plasma treatment and heating. The transferred membranes had a thickness in the range 60-80 nm, and were hydrophobic. The thickness of the transferred membrane could be controlled by varying the crosslinking and plasma treatment conditions. These conditions determine the penetration of oxygen into the PDMS, and hence the range over which the mechanical properties were transformed, which determines the location of the interfacial fracture plane and therefore thickness of the membrane. This method was used to fabricate residual-free patterns with controllable dimensions. This represents a facile and repeatable process to pattern surfaces with potential applications in areas of selective deposition of biological samples, such as cells, proteins, and DNA.

Chapter 3. Droplet Manipulation on the Magnetic Responsive Superhydrophobic Pillar Arrays

3-1. Introduction

Micro/nano fabrication technology to fabricate superhydrophobic surface has been over the remarkable development during last decades and many applications were developed not only superhydrophobic surface but also directional and switchable structures.[49-57] A lot of fabrication methods, including photolithography, micromolding and surface wrinkling have been employed to create the functional surfaces.[58-63] Recently, many researchers were interested in active structure beyond the passive functional structure. And on the strength of their efforts, many materials having switchable wetting properties response to external stimulations which are heat, light and magnetic force were discovered. Especially magnetic force responsive structure has been widely used to fabricate not only switchable wetting but also artificial mussel and controllable dry adhesive structure from its fast-responsive and controllable characteristics.

Kwon et al. fabricated magnetically programmed micro actuator which can be differently responded to magnetic force by anisotropy of magnetic particles. Through this structure they show the rotating, bending and moving of the actuator.

Del campo et al. suggested active gecko-inspired pillar structure where magnet particle was inserted into the polymer structure. Their adhesion force at original state decreases when the magnetic force is present because of bending of the pillars.[64]

Also, the magnetic responsive structure has been used for switchable wetting surface, which control wetting state of various liquids on the surfaces. Minko et al. demonstrated remote wetting control using superomniphobic re-entrant magnetic structures.[51] An external magnetic force was used to bend the re-entrant microstructures and simultaneously causes wetting transition from Cassie state to Wenzel state.

In contrast to those results, droplet manipulation using magnetic force responsive active structures is extremely rare. It is well established that the superhydrophobic surfaces with low adhesion and high mobility of droplets, which are estimated by static contact angles (CAs) and roll-off angles (ROAs), can be controlled by modifying texture and chemical treatment of surfaces according to the Wenzel and Cassie-Baxter models.[58, 62, 65-70] However, these superhydrophobic surfaces, usually consisting of high aspect ratio pillar arrays or rough hierarchical structures, are difficult to bend or response to external stimulations.

In this paper, we present a magnetic responsive droplet manipulation using magnetic particle embedded micro pillar arrays with high aspect ratio which are

robust and magnetic force responsive structures. To fabricate the active structures, we used composite of PDMS elastomer and magnetic particle. The mixture solution was sprayed to the PDMS substrate placed on the magnet, and then the composite pillar structure grows along the magnetic field direction. Heretofore, there are needed complicate photolithography, etching, wet process to make micro pillar structure,[71-73] but through this novel method, we could fabricate composite pillar array which has high aspect ratio (~10) without silicon fabrication methods. Also by ensuing carbon nanoparticles (CNPs) coating process, the pillars could have more superhydrophobic property.

We further demonstrate that the CAs and ROAs of droplets on the fabricated surfaces with/without external magnetic force according to the amounts the magnetic composite solution. Moreover, the interesting application of the droplet manipulation which is moving and collision test of droplets on the surfaces was demonstrated. Also deicing ability of the pillar by its own motion was represented.

3-2. Experimental

3-2-1. Fabrication of magnetic composite pillar

First, a base polymer of Sygard 184 (Dow Corning Korea, Seoul, Korea) and hexane (Sigma Aldrich Korea, Yongin-si, Korea) were mixed with a 1:1 weight ratio and vigorously stirred. Then, carbonyl iron particles (Sigma Aldrich Korea, Yongin-si, Korea) were added to the mixture with the same total weight as the PDMS base polymer. The mixture containing the carbonyl iron particles was sonicated for 30 min in a water bath. After the sonication, a curing agent of Sygard 184 was put in the solution at 10 wt% to the base polymer, and the solution was sonicated again. The composite solution was then spray-coated using a spray gun onto a cured PDMS substrate placed on a neodymium magnet (4 cm (W) \times 4 cm (L) \times 2 cm (T), maximum flux density: \sim 4 T, purchased from JL magnet, KOREA). The sprayed sample on the magnet was then placed in a convection oven for thermal curing for 2 h at 70 °C, which resulted in magnetically actuating self-assembled micropillar arrays. The micropillar arrays were spray-coated with 0.5 wt% CNPs (Sigma Aldrich) dispersed in 2 ml of acetone followed by 1 h drying at 70 °C, resulting in magnetically responsive hierarchical pillar arrays with superhydrophobicity.

3-2-2. Simulation of the magnetic field around the magnetically responsive film on a magnet

The magnetic field around the magnetically responsive film on a neodymium magnet was simulated using Finite Element Method Magnetics software (FEMM 4.2, <http://femm.foster-miller.net>). The simulation was conducted for two different types of magnets (a: 4 cm (W) \times 4 cm (L) \times 2 cm (T), maximum flux density: \sim 4 T and b: 2 cm (W) \times 2 cm (L) \times 1 cm (T), maximum flux density: \sim 3 T) operating in air.

3-2-3. Analysis of the structural change of the magnetically responsive pillar arrays under a magnetic field.

The magnetically responsive structural changes and actuating motions of the pillar arrays were investigated with upright optical microscopy by controlling the position of a neodymium magnet under the magnetically responsive film. The magnetically responsive film with randomly oriented pillar arrays was attached to a flat glass slide to prevent bending of the film. The position of the film was controlled by a manual 3-axis stage, and the dynamic responses of the pillar arrays were captured with a CCD camera attached to the microscope.

3-2-4. Analysis of wetting properties of the magnetically responsive pillar arrays

The static CAs and advancing/receding CAs were measured using a contact angle analyser (Drop Shape Analysis System DSA100, Kruss, Germany). The 10 ~30 μl deionized (DI) water droplets were gently placed on the magnetic pillar arrays for static CA measurement. The advancing/receding CAs were measured by smoothly increasing and decreasing the volume rate of the DI water droplet. The droplet images were captured by an optical microscope on the contact angle analyser. The ROA was determined by slowly tilting the substrate until a droplet started to roll off and recording the angle of the substrate at that instant.

3-2-5. Manipulation of droplets on the magnetically responsive film

A 10 μl DI water droplet was placed on a magnetically responsive film fixed on a glass slide. A neodymium magnet was located right under the droplet. The magnet was then moved to a specific target location. As the magnet moved towards the location, pillar arrays immediately ahead of the magnet laid flat against the substrate. As a result, the droplet rolled over the bent pillars, following the magnet. The motion of the droplet was recorded using a digital camcorder.

3-2-6. Analysis of anti-icing property of the magnetically responsive film

A magnetically responsive film with 10 μl of deionized water droplets on the surface was placed in a refrigerator at $-10\text{ }^{\circ}\text{C}$ for 2 hours to completely freeze the droplets. Then, a neodymium magnet was moved under the film to actuate the magnetically responsive pillar arrays. Detachment and removal of the iced droplets from the surface were captured using a digital camcorder.

3-3. Results and Discussion

3-3-1. Preparation of magnetically responsive film

Among many possible approaches to generate dynamically tuneable structures, magnetically actuated surfaces are particularly attractive due to their instantaneous response and remote controllability and the nondestructive nature of magnetic fields. Figure 3-1 depicts in detail the procedure for the preparation of a magnetically responsive film with self-assembled hierarchical pillar arrays on the surface. First, a solution of magnetic particles and polydimethylsiloxane (PDMS) was prepared by adding carbonyl iron (CI) particles into a mixture of uncured PDMS and hexane. Then, 1.5 ml of the solution was sprayed using a spray gun onto a cured PDMS substrate that was placed on a neodymium magnet. Then, the mixture of ferromagnetic CI particles and uncured PDMS spontaneously arranged along the direction of the magnetic field and formed pillar-like structures. Subsequent thermal curing of the sprayed samples fixed the field-aligned pillar shapes, resulting in composite pillar arrays made of PDMS and magnetic particles over a large area; the magnetic particles in the pillars enabled dynamic tuning of structural motions, whereas the polymeric matrix defined the structural geometry (Figure 3-1b-d). The coating of carbon nanoparticles (CNPs) over the arrays resulted in magnetically actuating hierarchical pillar arrays with

superhydrophobicity. Previous studies have shown that well-defined magnetically responsive structures can be generated via photolithographic or soft lithographic techniques, in which pre-defined masks or moulds were applied to precured polymers mixed with magnetic particles[74-76]. Although these methods are useful to fabricate magnetically responsive surfaces with ordered micro- or nanoscale structures, additional lithographic processes to prepare the mask or mould are required. Additionally, instantaneous modulation of geometries of magnetically responsive structures is not possible with these mould-based approaches, because the geometries of the resulting samples are usually limited by the patterns of the masks or moulds.

By contrast, pillar geometries can be simply tuned in our approach by the modulation of a magnetic field. As shown in Figure 3-2a, the magnetic flux density varies with the distance between the substrate and the magnet. Therefore, pillar arrays with different diameters and heights can be generated by controlling the distance between the substrate and the magnet during the fabrication procedure (Figure 3-3). For example, when the substrate is placed on the magnet without a gap between them, the average height of the micropillars was maximized to $\sim 580 \mu\text{m}$. By increasing the distance between the substrate and magnet, the height was decreased and reached $\sim 380 \mu\text{m}$ at a separation of 25 mm (Figure 3-2b). By contrast, the diameter of the pillar arrays was reduced to $\sim 70 \mu\text{m}$ when the separation was zero and monotonically increased with the distance,

reaching $\sim 210 \mu\text{m}$ at a distance of $\sim 25 \text{ mm}$ (Figure 3-2c). This is because the solution containing magnetic particles experiences higher magnetic field density and strength when the separation is minimized. The height and diameter of the pillar arrays can also be modulated by repeating the process of spray coating-curing (Figure 3-4). When the coating-curing process was performed only once, the height and the diameter of the pillars were $\sim 500 \mu\text{m}$ and $\sim 90 \mu\text{m}$, respectively. During this process, the distance between the sample and the magnet was maintained at zero, and the amount of mixture sprayed in a single coating was $\sim 1.5 \text{ ml}$. By repeating this process, the height and diameter were increased, as shown in Figure 3-2d and e. After the third coating and curing process, the height reached $\sim 1300 \mu\text{m}$ and the diameter was increased to $\sim 130 \mu\text{m}$, generating pillar structures with a very high aspect ratio (>10). The pillar geometry can also be adjusted by controlling the amount of sprayed mixture on the PDMS substrate (Figure 3-5). When we sprayed 0.5 ml of the mixture, a pillar array with relatively low density and height was generated. When we increased the amount during spraying, micropillar arrays with higher density and height could be generated. The generated micropillars with controllable geometries can be further modified into micro- and nanoscale combined hierarchical pillar arrays by coating the micropillars with CNPs, which provide the array with thermodynamically stable superhydrophobicity. With simple tunability of the structural geometries, including diameter, height, and hierarchy, of the pillar arrays, our approach

provides a novel strategy for generating magnetically responsive hierarchical pillar arrays with robust superhydrophobicity over a large area by simple self-assembly without the need for complex fabrication processes or predefined moulds.

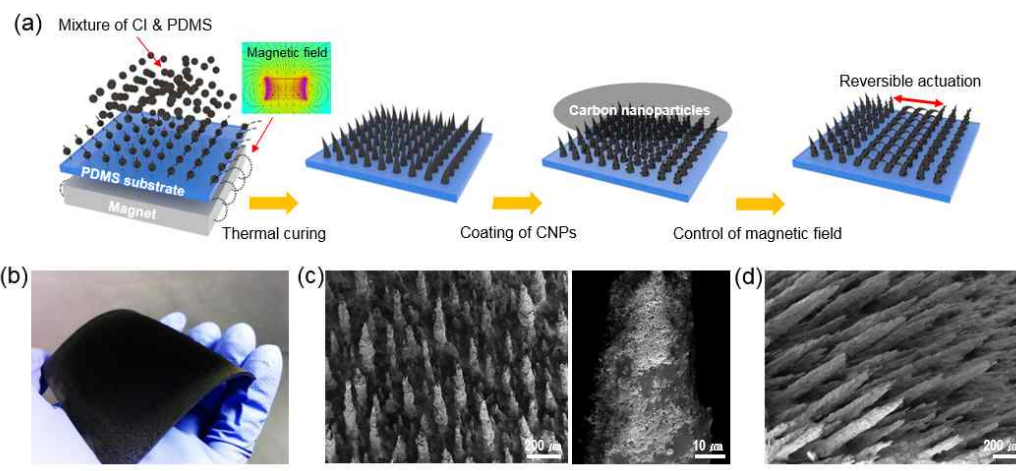


Figure 3-1. Schematic illustration of pillar fabrication.

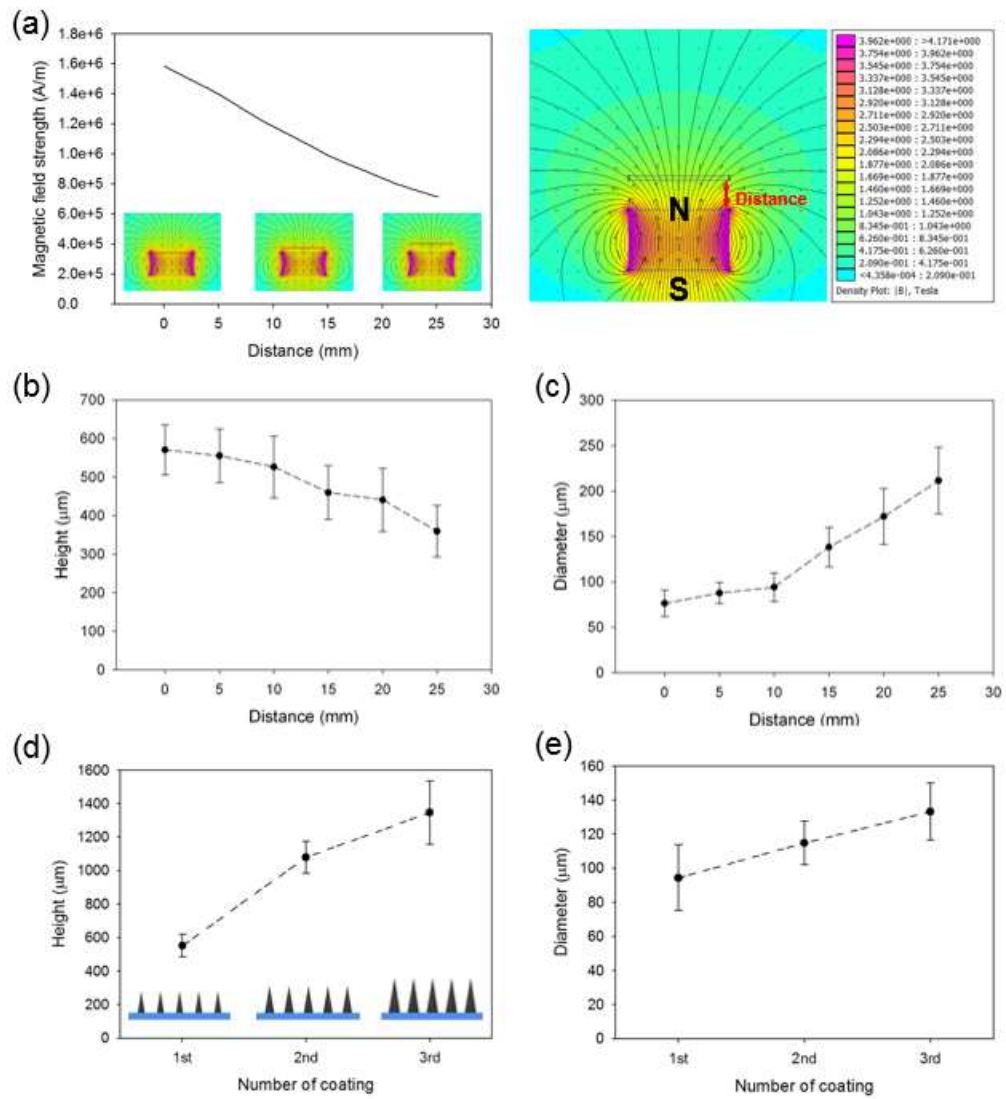


Figure 3-2. (a) Magnetic field simulation as distance with magnet. (b)-(c) Height and diameter change by increasing of distance with magnet. (d)-(e) Height and diameter change by number of coating.

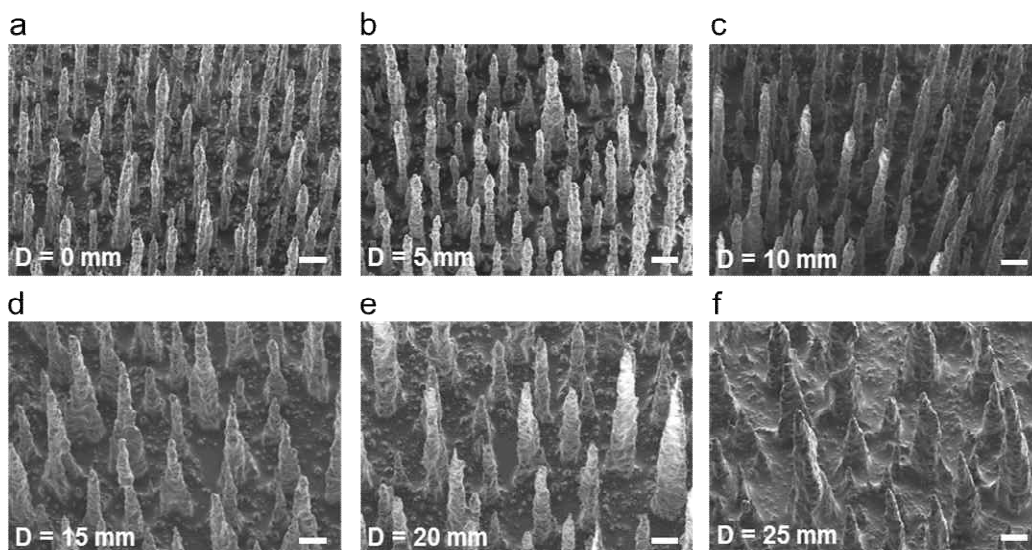


Figure 3-3. SEM images of the fabricated magnetically responsive pillars as a function of distance (D) between the magnet and the sample. a. D = 0 mm, b. D = 5 mm, c. D = 10 mm, d. D = 15 mm, e. D = 20 mm, f. D = 25 mm. Scale bars in (a)-(f) are 200 μm.

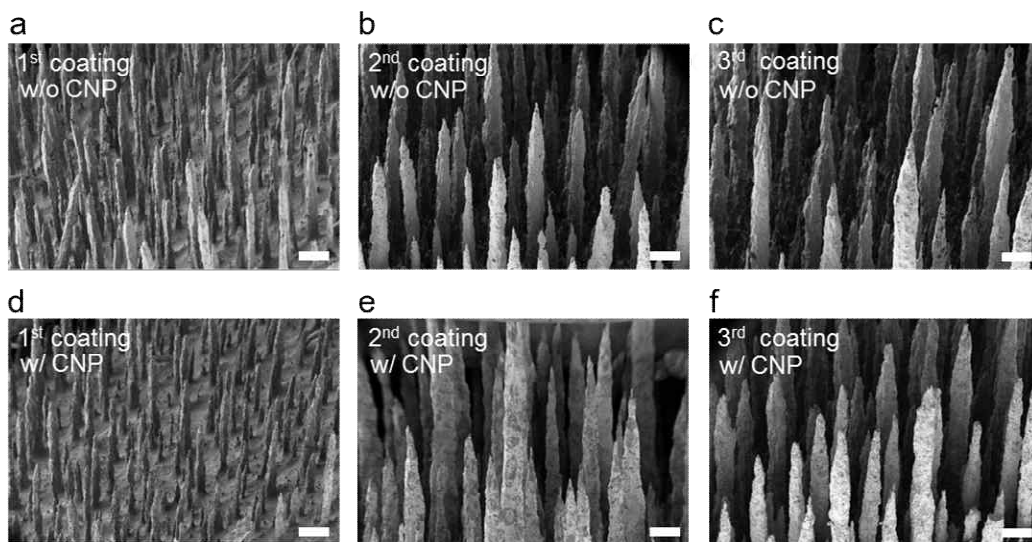


Figure 3-4. SEM images of the fabricated magnetically responsive pillars as a function of the number of coating-curing processes. (a)-(c) are samples without CNP coating and (d)-(f) are samples with CNP coating. Scale bars in (a)-(f) are 200 μm.

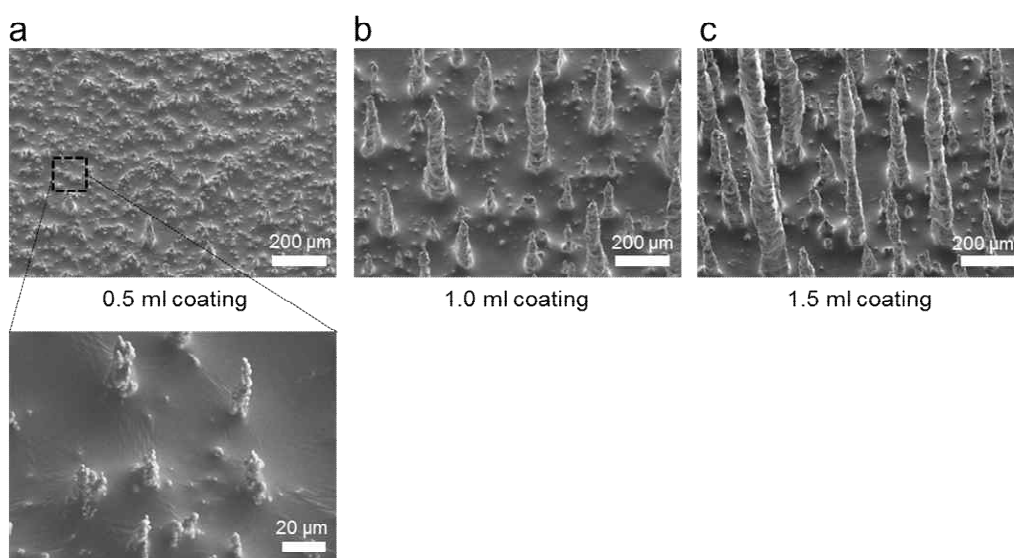


Figure 3-5. SEM images of the magnetically responsive pillar arrays prepared using different amount of sprayed mixture comprising of precured polymers and magnetic particles. 0.5 ml, 1.0 ml and 1.5 ml solutions were used for the resulting samples in (a), (b), and (c), respectively.

3-3-2. Active control of the dynamic structural change of the magnetic pillar arrays by an external magnetic field

To investigate the dynamic response of the pillar arrays under a magnetic field, structural changes of the pillar were observed with upright optical microscopy by changing the horizontal position of a rectangular neodymium magnet under the films. When the rectangular magnet is placed under the film, the magnetic flux density is maximized at the centre and rapidly decreased with the distance from the centre (Figure 3-6). Consequently, pillars located directly above the magnet undergo the strongest magnetic field, whereas pillars located away from the boundaries of the magnet are under little influence of the field. This indicates that the bending and actuating behaviours of the array can be simply and precisely controlled by changing the location of the magnet under the sample. For example, when we placed a rectangular magnet (2 cm (W) \times 2 cm (L) \times 1 cm (T), and the maximum flux density: \sim 3 T) 6 mm away from the south or north pole face of the magnet (defined as “d” in Figure 3-6a), the pillars maintained their original vertical position without any bending (Figure 3-6b). However, as the magnet approached the sample, the pillar arrays started to respond strongly to the magnet because of the highly ferromagnetic carbonyl iron. When the distance was \sim 4 mm, the array bent to a tilting angle of \sim 60°. As the distance decreased, the magnetic

flux density influence on the pillar array increased, resulting in more bending. Furthermore, the pillar array was nearly flattened to the surface with tilting angles of $\sim 90^\circ$ when the horizontal distance between the side of the magnet and the sample was zero. When the magnet was removed, the arrays immediately returned to their original vertical position by the elastic restoring force of the PDMS matrix (see Figure 3-7), demonstrating fast and reliable actuating, as well as large bending capability, in response to a remote magnetic force. Figure 3-6c shows top views of the magnetically responsive pillar array placed over a rectangular magnet. As shown, only the pillars located directly above the magnet were significantly bent, whereas pillars beyond the magnet's face showed little or no bending. The pillars located at the edges of the magnet were bent towards the centre of the side face of the magnet along the magnetic field formed between the north (N) and the south (S) pole faces of the magnet. When we rotate the magnet under the film, the direction of the bent pillars also changed along with the magnet (Figure 3-6c).

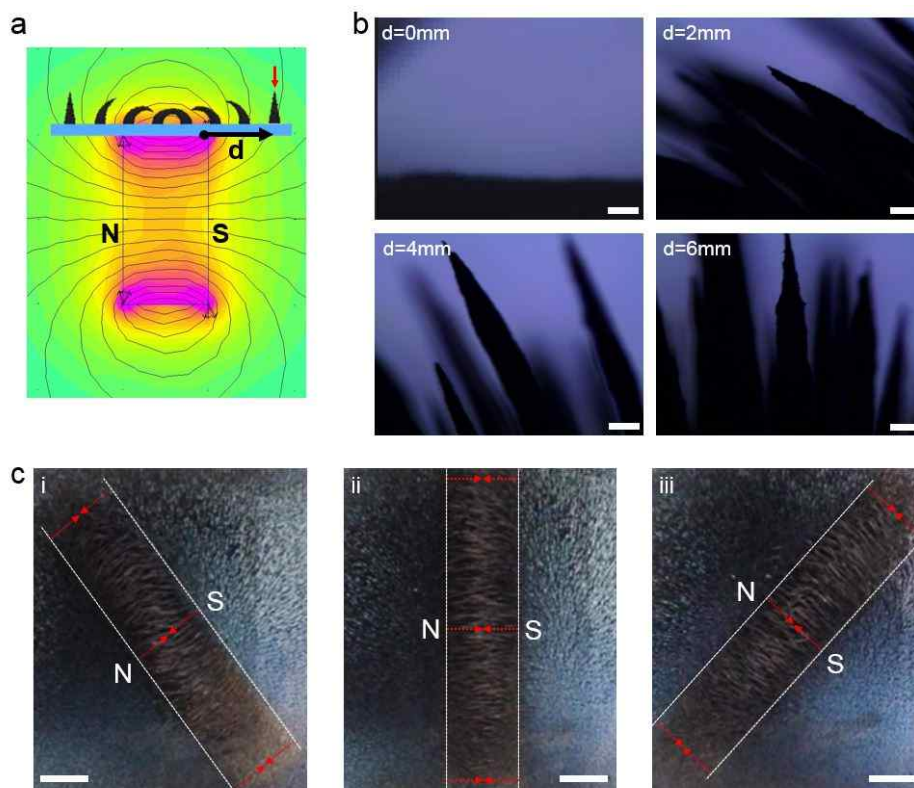


Figure 3-6. Dynamic structural control of the magnetically responsive pillar array with a permanent magnet. (a) Simulation of magnetic flux density around the pillar array when a magnet is placed under the sample. (b) Side views of the dynamic response of the pillar array when the magnet approaches the targeted pillars (red arrows in Fig. 3a) at a horizontal distance “d” from the edge of the magnet. Scale bars are 200 μm . (c) Top-views of the magnetically responsive pillar array placed on a rectangular magnet. The pillars located directly above the magnet are significantly bent. The region of bent pillars rotates along with the magnet. Scale bars are 1 cm.

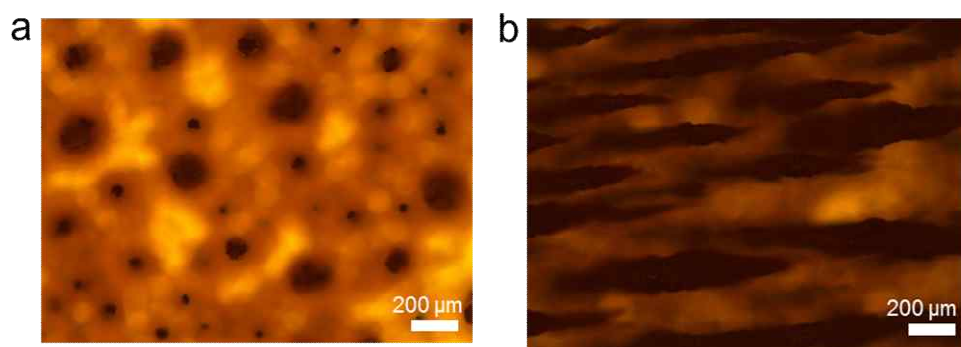


Figure 3-7. Top-views of the magnetically responsive pillar arrays (a) with and (b) without applied magnetic field.

3-3-3. Wetting properties of the magnetically responsive film

From The surface wetting properties of the arrays related to the CNP coating and the number of coating-curing processes were investigated. The CNP coating adds structural hierarchy to the pillar arrays (Figure 3-8a), and the repetition of the spray coating-curing process increases the diameter and the height of the pillar arrays, as described above. For pillar arrays in their original unbent configuration, arrays with more coating-curing processes exhibited higher contact angles (CA) and reduced contact angle hysteresis (CAH) (Figure 3-8b). This is because the air fraction under the droplet is increased for the samples with more spray coating-curing processes (Figure 3-9). Furthermore, coating of the array with CNPs significantly enhanced $CA > 150^\circ$ and reduced $CAH < 10^\circ$, enabling superhydrophobic wetting (Figure 3-8b) by introducing dual roughness to the array [68, 69] [77].

When the pillar arrays were bent under a magnetic field, different wetting behaviours were observed depending on the presence of CNPs on the arrays. For example, arrays without CNPs showed decreased CAs with increasing spray coating-curing processes (Figure 3-8c). CAs on the arrays prepared with a third coating process reduced to $\sim 123^\circ$. Additionally, the bent pillar arrays without CNPs showed a relatively high CAH of over 23° , which could hinder the manipulation of droplets on the arrays. This is due to the increase in solid fraction

under the droplet for samples with more coating-curing processes when the arrays without CNPs are bent under a magnetic field (Figure 3-10). By contrast, pillar arrays with CNP layers showed enhanced CAs with increasing coating-curing processes (Figure 3-8c). Interestingly, these arrays maintained their superhydrophobicity (CAs $> 150^\circ$ and CAH $< 10^\circ$) even when the arrays were bent by a magnetic force. This is because the CNP coating creates nanoscale roughness over the surface of the micropillars, resulting in micro- and nanoscale combined hierarchical structures. These hierarchical architectures enable the array to maintain reduced contact with the droplet and thus a superhydrophobic wetting state regardless of the bending angle of the pillar arrays. These results indicate that a discrete droplet would not wet these self-assembled hierarchical pillar arrays even when the arrays are actuating under a magnetic force, which may enable active and reversible manipulation of a droplet on the pillar arrays. Although previous studies have reported droplet manipulation based on magnetic force, they are mostly limited to demonstrating the transition of the wetting state from the Cassie-Baxter state to the Wenzel state upon actuation or bending of micro- or nanoscale structures. In this case, not only is the wetting transition irreversible, but precise and fast control of the position and motion of discrete droplets is also not possible.[51, 74, 78] By contrast, our results demonstrate a strong possibility of rapid and reversible control over the position and motion of droplets using magnetically actuated surfaces.

To further characterize the wetting properties, we also measured the roll-off angles (ROAs) of a droplet on the pillar array, which were determined as the tilting angles of the substrate at which the droplet starts to roll off[65]. The ROA of a vertical pillar array without CNPs fabricated with a single coating-curing process was $\sim 59^\circ$. The ROA decreased to $\sim 30^\circ$ for triple coated samples. By coating CNPs on the pillars, the ROA dramatically decreased to $\sim 17^\circ$ for single coated samples and further decreased to $< 10^\circ$ for triple coated samples (Figure 3-8d). Interestingly, when we applied a magnetic field to the samples, the ROAs of the pillar arrays were greatly reduced. The ROAs of the pillars without CNPs were 22° , 18° and 12° , respectively, with increasing spray coating-curing processes. Strikingly, pillar arrays coated with CNPs shows ROAs of $\sim 0^\circ$ when bending under a magnetic force (Figure 3-8d and Figure 3-11). This means that these arrays have a strong potential to transport and manipulate a liquid droplet on the surface with only a remote magnetic field and without the need for inclining the substrate.

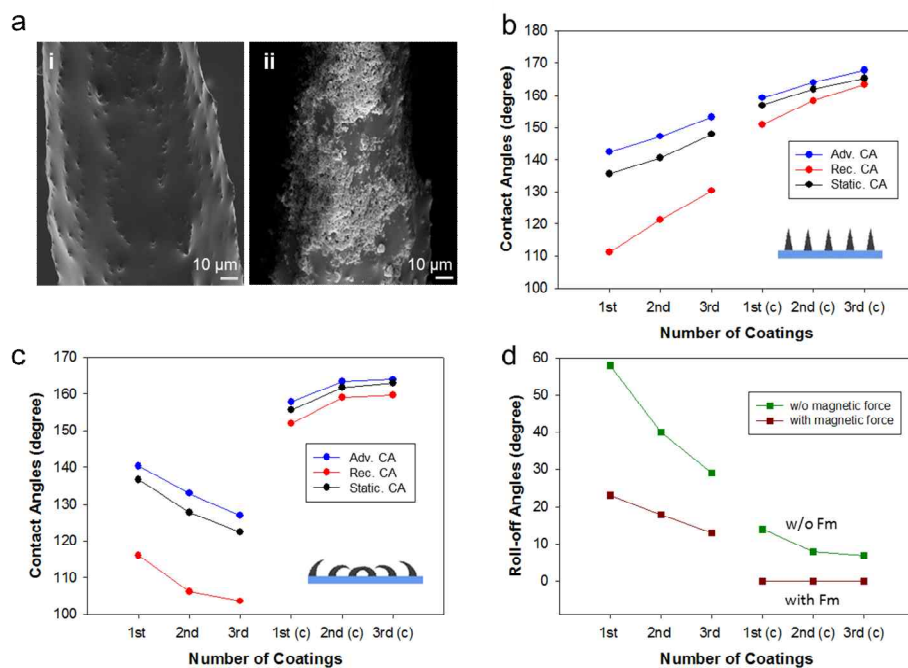


Figure 3-8. Analysis of the wetting properties of the magnetically responsive pillar arrays. (a) SEM images of a pillar without (left) and with (right) CNP coating. **(b)** Contact angles of DI water on various magnetically responsive pillar arrays with different numbers of coating-curing processes when no magnetic field is applied to the sample. **(c)** Contact angles of DI water on various magnetically responsive pillar arrays with different numbers of coating-curing processes when the pillar arrays are fully flattened on the substrate by an applied magnetic field. **(d)** Roll-off angles of DI water on various magnetically responsive pillar arrays for different numbers of coating-curing processes and magnetic field application. The symbol “(c)” on the x-axis of the graphs in (b)-(d) represents CNP coated samples.

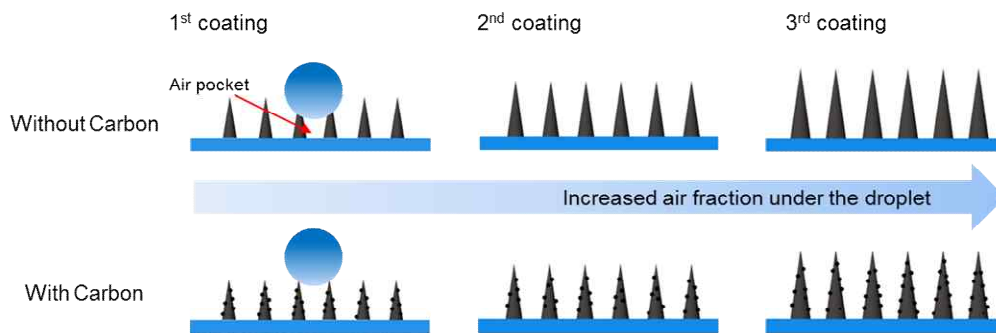


Figure 3-9. Schematic illustration of droplet wetting on various magnetically responsive pillar arrays related to the CNP coating and the number of coating-curing processes when no magnetic field is applied to the samples.

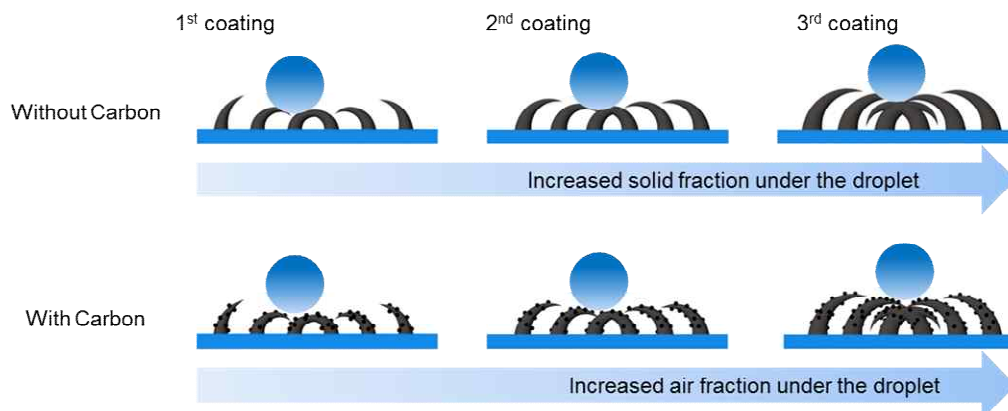


Figure 3-10. Schematic illustration of droplet wetting on various magnetically responsive pillar arrays related to the CNP coating and the number of coating-curing processes when the pillar arrays are bent by an applied magnetic field.

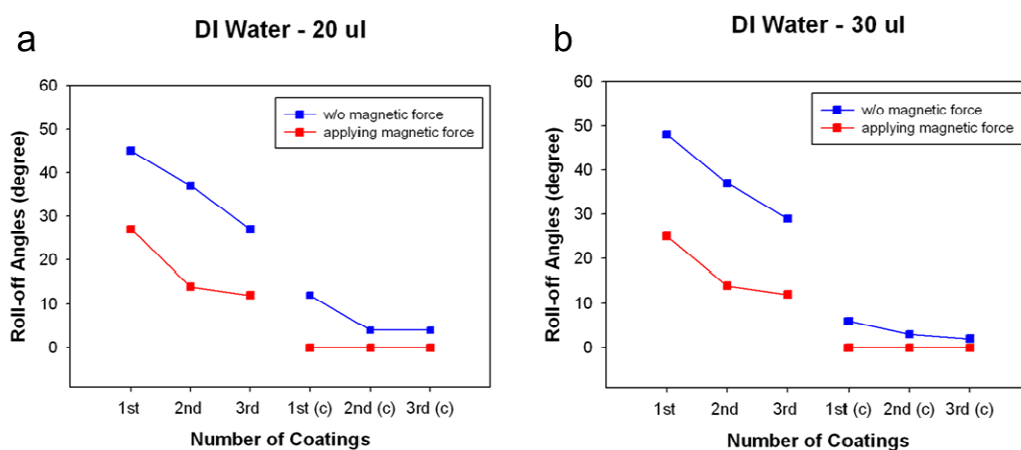


Figure 3-11. Roll-off angles of DI water with two different droplet volumes on various magnetically responsive pillar arrays for different numbers of coating-curing processes and magnetic field application. The symbol “(c)” on the x-axis of the graphs in (a)-(b) represents CNP coated samples.

3-3-4. Remote manipulation of droplets on the magnetically responsive film

Figure 3-12a shows an illustration of droplet manipulation on our flexible magnetically responsive film. When pillars above the magnet are bent, a local difference in the potential energy is generated in the array. Furthermore, actuation of the pillars provides a driving force for the droplet to move along the tilting direction of the pillars. As a result, the droplet moves towards the location of the bent pillars. Figure 3-12b shows the continuous manipulation of a droplet on the CNP coated pillar arrays. A 10 μl DI water droplet was placed on the magnetically responsive film fixed on a slide glass. A neodymium magnet was moved under the substrate. As the magnet approached the array, pillars within the magnetic field flattened on the substrate. As a result, the droplet rolled over the bent pillars, following the magnet. Consistent with our earlier results, the droplet maintained a superhydrophobic wetting state on the pillar arrays regardless of the bending angles of the array. The pillars in the places where the magnet passed recovered their original vertical shape, whereas the magnet bent pillars further down the path. This series of subsequent local actuating of pillar arrays by controlling a magnetic field enabled precise and active manipulation of the droplet.

As shown, our self-assembled pillar arrays not only exhibit magnetically responsive dynamic behaviours but also have highly stable superhydrophobic wetting properties with a nearly zero ROA upon the application of an external

magnetic field. This unique property is of considerable benefit for the active manipulation of liquid droplets. To demonstrate unique applicability, we guided the transportation of a water droplet to a specific target location using only remote magnetic force (Figure 3-13a). Initially, 10 μ l of three DI water droplets dyed with different colours (blue, yellow and red from left) were placed on the flexible film. Due to the superhydrophobicity of the film, each droplet maintained discrete spherical shapes on the film. The blue coloured droplet was moved to the right side until it contacted the yellow droplet by simply placing a permanent neodymium magnet under the blue droplet and moving the magnet to the right. The droplet maintained its superhydrophobic state during the motion with very low CAH. After contacting with the yellow droplet, the two droplets merged together, generating a larger green droplet. Similarly, the merged droplet was successfully transported to the red droplet, forming another merged droplet using just a remote magnetic field. It should be noted that this is the first demonstration of active and reversible manipulation of the position and motion of pure discrete droplets using only a remote magnetic field. So far, the active control of discrete droplets has mainly been achieved by electrowetting methods, which utilize electric fields applied to patterned electrodes. Most previous droplet manipulation techniques based on magnetic fields are limited to irreversible wetting transitions from the Cassie-Baxter state to the Wenzel state upon the bending of micro- or nanostructures without the ability to control the position and motion of discrete

droplets.[51, 74, 78] With the dynamically actuating pillar arrays under a controlled magnetic field, our approach combines the major advantages of electrowetting (i.e., active real-time manipulation of a droplet to a specific target location) and structure-based methods (i.e., simple processes and no need for an external power source).

To demonstrate controllability over droplet motion and position, we performed an additional experiment (Figure 3-13b). First, we placed the magnetically responsive flexible film on the table with a slight tilting angle of $\sim 5^\circ$. Then, a permanent magnet was placed under the film while a water droplet dyed with red colouring was drop dispensed onto the film. Pillars under the influence of the magnetic field tilted along the magnetic field direction, forming an open channel on the magnet. As a result, the droplet rolled off towards a specific target location along the channel. The channel direction could be easily tuned by rotating the magnet. In addition to droplet manipulation, this magnetically responsive film with superior wetting properties is also highly useful for anti-icing surfaces. Because of the superhydrophobic wetting properties, ice particles would form with nearly perfect spherical shapes on the surface. These ice particles could be simply removed from the surface by actuating the pillar arrays with a magnet (Figure 3-13c).

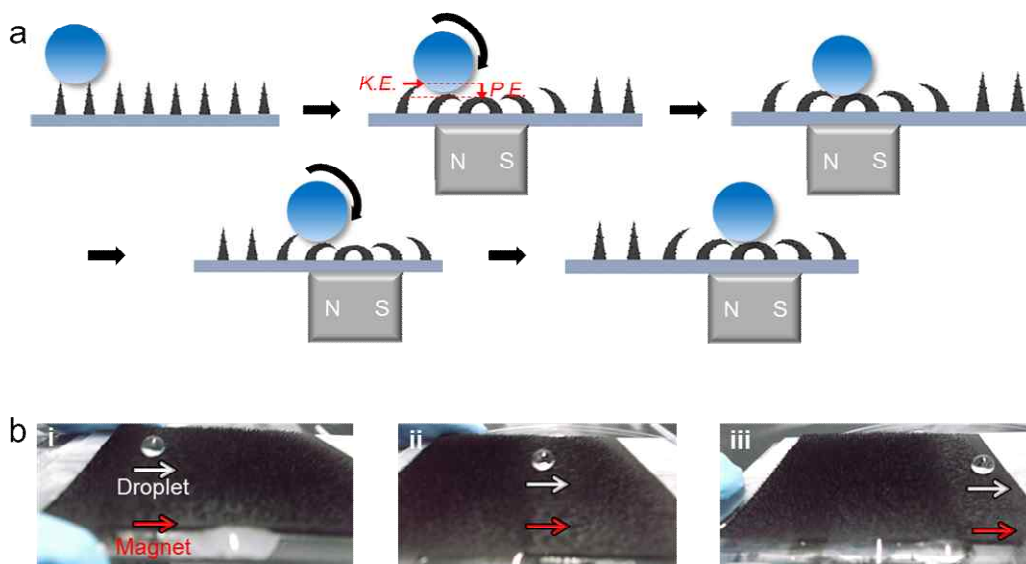


Figure 3-12. Droplet manipulation on the flexible magnetically responsive film. (a) Schematic illustration of active droplet manipulation on the magnetically actuating hierarchical pillar array. When the pillars are bent by a magnetic force, a local difference in the potential energy (“PE”) is generated in the array. Furthermore, actuation of the pillars provides a driving force (kinetic energy, “KE”) for the droplet to move along the direction of the pillars. As a result, the droplet moves towards the location of the bent pillars. (b) Demonstration of continuous manipulation of the droplet on the magnetically responsive film with a neodymium magnet.

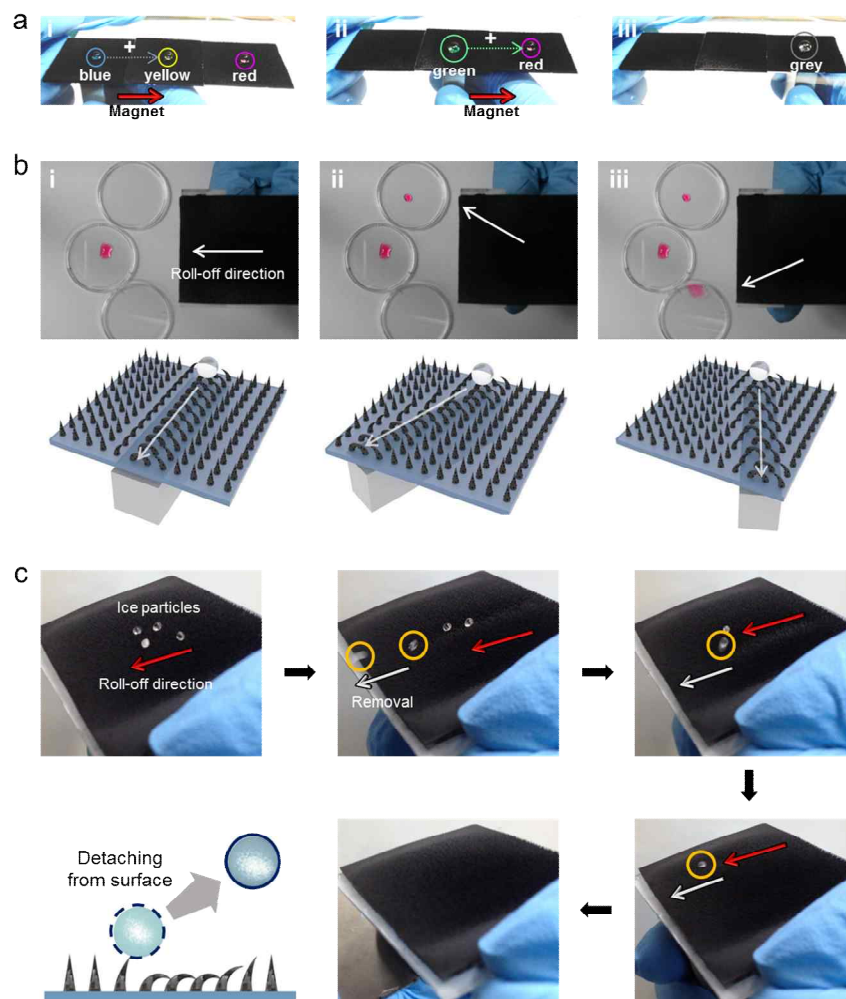


Figure 3-13. Applications of the magnetically responsive film with superhydrophobic wetting properties. (a) Demonstration of precise manipulation of droplets to specific targeted locations. A blue coloured droplet is manipulated with a permanent neodymium magnet to the right until it contacts the yellow droplet. After contacting the yellow droplet, the two droplets merge together, generating a larger green droplet. The merged droplet is further

transported using the magnet to the red droplet, forming another merged droplet.

(b) Guided rolling-off of the droplet to targeted locations. Pillar arrays on a magnet are flattened on the substrate along the magnetic field direction, forming an open channel on the surface. As a result, a droplet can be rolled off towards a specific target location along the channel. The channel direction can be easily tuned by rotating the magnet. **(c)** Demonstration of anti-icing properties of the film. Because of the superhydrophobic wetting properties, ice particles form with nearly perfect spherical shapes on the film. These ice particles can be removed from the surface simply by actuating the pillar arrays with a magnet.

3-5. Summary

In the present study, we have presented, for the first time, a novel strategy that enables active, fast, precise and reversible control of the positions and motions of pure discrete droplets using only a permanent magnet on a magnetically responsive flexible film. The magnetic responsive film has randomly oriented hierarchical pillar arrays on the surface generated by the mouldless self-assembly of solutions comprising precured polymers and magnetic particles under a magnetic field. The geometries of the pillar arrays, such as diameter, height and density, can be tuned simply by controlling the magnetic field during the fabrication process. These magnetically responsive pillar arrays not only have dynamic actuating capabilities with immediate field responses and maximum tilting angles of $\sim 90^\circ$ but also exhibit stable superhydrophobic wetting properties regardless of the bending angles of the actuating pillar arrays. With these superior actuating and wetting properties, this flexible film enables active, fast, precise and reversible manipulation of discrete droplets on the surface with the use of only a permanent magnet without any additional processes or equipment. Furthermore, the fabrication of this flexible film is scalable through the simple self-assembly process without the need for any expensive processing or materials. We believe that this new magnetically responsive flexible film provides a valuable platform for active and precise manipulation of liquid droplets for a broad range of

applications, from lab-on-a-chip devices for biological and chemical analyses to bioinspired functional surfaces.

Chapter 4. Fabrication of Solid Oxide Fuel Cell via Electrospray method

4-1. Introduction

Solid Oxide Fuel Cell (SOFC) is a promising energy generation system because of high efficiency, low pollutant and diversity of fuel materials. The general operating temperature of the SOFC is 600°C ~ 800°C, and waste heat from the high temperature can be converted to other energy. Aside from hydrogen, hydrocarbon based materials can be used for fuels as well.

The general SOFC consists of an anode, an electrolyte and a cathode. The air and hydrogen is provided to the cathode and anode respectively, and the electrolyte have to be fully dense to protect the gas diffusion. Anode-support or electrolyte-support type SOFCs are mostly used for cell fabrication and there are some properties that should be considered.

At the cathode, oxygen reduction occurs, which generates ion moves to the anode through the electrolyte. The reaction between oxygen ion and hydrogen generates water molecule and electrons. Therefore, the cathode and the anode need to have high ion and electronic conductivity but electrolyte have high ion conductivity and low electrical conductivity. Also the structure of the cathode and

the anode have to be porous for gas diffusion, and all the components are required to have similar thermal expansion coefficients for thermal stability.

Various fabrication processes are developed to make the components of the SOFC. Screen printing has been widely used for the fabrication of electrolyte and cathode materials. However, since it is hard to make thin layer and control structure of the components, other deposition methods such as Pulsed Laser deposition (PLD), Atomic Layer Deposition (ALD) and Sputtering have been developed as alternatives and they are also used with the combination of the screen printing method.[79-81] Those methods can fabricate thin electrolyte and cathode layers precisely with high quality, but they have problems such as difficulties in realizing proper circumstances and limitations in manufacturing over large area.

In this chapter, we present a fabrication process of the components of SOFC using electrospray deposition (ESD) method. The electrospray deposition method (ESD) is a simple and versatile tool for uniform particle deposition. In the ESD process, the liquid jet at a syringe is divided into nano-sized droplet by induced voltage, then the droplets are sprayed on the target substrate by electrical potential.[82-84] The ESD method can manufacture higher quality particle film layers than other spray methods such as air assist, rotary and ultrasonic atomization because droplets expelled by coulomb fission are very uniform and have narrow size distribution. The morphology of deposited particles depends on

various conditions such as solution properties and process variables. The solution properties (viscosity, conductivity, surface tension, evaporation temperature) which affect the shape of particle layers are influenced by not only solvents but particles and dispersant polymer. The shape of the liquid jet and the size of droplets are also changed by process variables (voltage, flow rate and distance).

The ESD process can be used under the atmospheric environment, and the diverse materials can be selected as the substrate. From those advantages, it is possible to fabricate components of the SOFC, which are the electrolyte and the cathode layer. Also, we can control and optimize the structure of SOFC components using polymer binders.

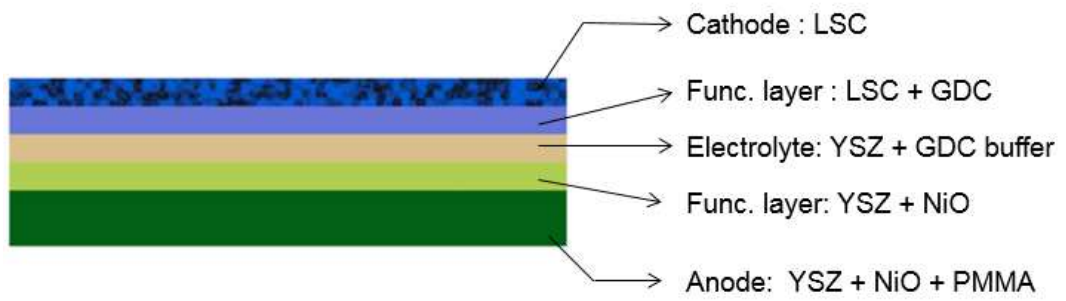


Figure 4-1. Schematic diagram of the SOFC.

4-2. Experimental

4-2-1. Materials and Electrospray set-up

The NiO-YSZ substrate was processed by powder pressing method using (Granule material). Electrospray machine which consist of power supply, syringe and controller was made by Nano-NC tec. 8 mol % Y₂O₃ stabilized ZrO₂, 8YSZ and LSC powder were used as electrolyte and cathode layer respectively, and they dispersed in ethanol for spray process. Liquid flow rate was 0.5ml/h, and voltage was applied with 10 kV ~ 11 kV range for uniform cone-jet mode. Ethanol and DI water was used for the dispersion liquid and polyvinyl pyrrolidone and polyvinyl butyral was added to the solution as binder and dispersant.

4-2-2. Sintering process

YSZ deposited NiO-YSZ substrate was co-fired at 1400 °C during 5 h. GDC buffer layer was co-fired at 1250 °C during 2 h and then LSC cathode sintered at 1000 °C during 1 h. Those sintering process was conducted in air condition.

4-2-3. Electrochemical and structure analysis of the cell

At the cell operation, air and humified H₂ (3% H₂O) were supplied as the oxidant and fuel respectively with 200 sccm flow rate. A Solatron impedance analyzer with electrochemical equipment (SI1260 and SI1278) and Iviumstat electrochemical analyzer (Iviumstat, Ivium Technology) were used to obtain electrochemical impedance spectra (EIS) and current-voltage-power (I-V-P) curves. The analyzed temperature were 650 ~ 500°C with 50°C intervals and the frequency range was from 10⁶ to 10⁻¹ HZ.

4-3. Results and Discussion

4-3-1. Electrospray deposition process for fabrication of SOFC component

When the voltage was applied to the needle, the solution is atomized to the small droplets which make high quality film on the substrate. We chose anode-supported, planar type cell for ESD process and the substrate was fabricated by conventional power process. High voltage (8 ~ 12 kV) was connected to spray nozzle, the particle/polymer composite deposited to grounded substrate. Flow rate was controlled by step motor push the syringe.

During deposition process, the polymer binder not only makes good adhesion between the substrate and the particles but also help mass transportation of the particles during annealing process. The dispersion state of the solution varied by the amount of the polymer dispersant, and the morphology of the annealed particles become different by the polymer.

In this report, structure of the deposited film was modulated by dispersant/binder polymer and the condition to get well defined electrolyte layer and porous electrolyte/cathode layer was studied.

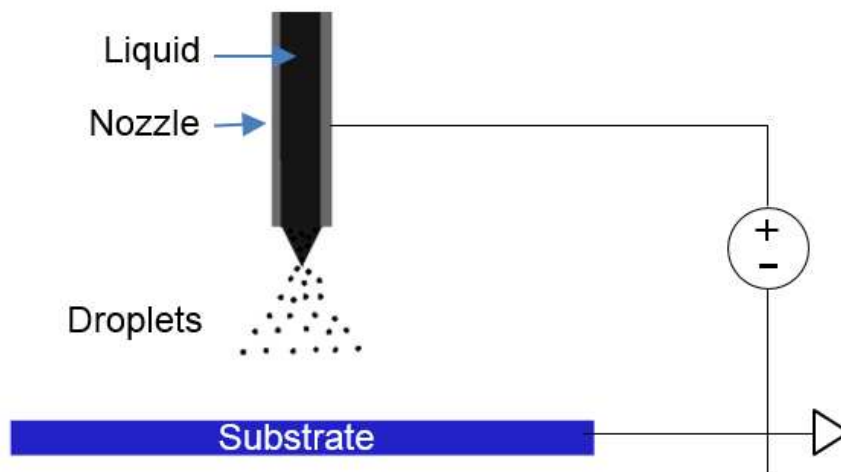


Fig 4-2. Schematic illustration for ESD process

4-3-2. LSC cathode deposition using electrospray deposition and electrochemical analysis

The LSC is promising perovskite material for intermediate temperature SOFC.[85] We used the LSC commercial powder for the cathode of the SOFC via electrospray process and optimized the structure of LSC using polymer dispersant.

For ESD process, 10 wt% of the LSC was dispersed in ethanol using bath sonication. PVP polymer was also added to the solution as dispersant. As-prepared NiO-YSZ substrate was made via pressing process followed by screen printing method for electrolyte layer. Then the LSC/GDC functional layer assists adhesion between electrolyte and cathode layer was deposited followed by LSC cathode deposition. Supplied voltage was 10 kV, flow rate was 0.3 ml/h, nozzle diameter was 25G (250 μm) and the distance between nozzle and substrate was 5 cm. We deposited the 1 μm CFL, then piled up the 2 μm LSC layer on the CFL.

In the ESD process, amount of the PVP morphology of the LSC layer. Figure 4-3 shows the SEM image of the CFL/LSC layer deposited by ESD with different PVP weight ratio. When the quantity of PVP is half of that of LSC, it can be found that lager ball shape of LSC was deposited because dispersion state of LSC is not sufficient (Figure 4-3a). As more PVP was added, more uniformly deposited LSC was found (Figure 4-3b) and then the 20 wt% PVP case, irregular fiber is generated (Figure 4-3c) because of the high viscosity of the solution.

To confirm performances of the LSC layers which have different shape, we conducted electrochemical analysis about two cases which are LSC : PVP = 10 : 5 (L2P1), LSC : PVP = 10 : 10 (L1P1) and 10 : 20 (L1P2). Figure 4-4 represents electrochemical performances of those samples. Their open circuit voltage (OCV) was > 1.13 V, and it means electrolyte has sufficient gas tightness. The peak power density of L2P1, L1P1 and L1P2 was 312 mW/cm^2 , 401 mW/cm^2 and 314 mW/cm^2 at $650 \text{ }^\circ\text{C}$. Though L2P1 has higher porosity, larger particle assembled structure decreases the reaction site of LSC which influence performance of cathode. Meanwhile, more voids are observed in L1P2 because of irregular polymer fiber, and the loss of cathode area by the voids decrease the performance of the cell. The impedance spectra under OCV condition are represented in figure 4-5. The area specific ohmic resistance (R_Ω) can be obtained from high frequency intercept and the polarization resistance (R_p) analyzed by subtracting the high frequency intercepts. The R_Ω of the L2P1, L1P1 and L1P2 were similar as $\sim 0.4 \text{ } \Omega \cdot \text{cm}^2$ at $650 \text{ }^\circ\text{C}$, But R_p of L1P1 and L1P2 were $3.1 \text{ } \Omega \cdot \text{cm}^2$, $1.7 \text{ } \Omega \cdot \text{cm}^2$ and $2.2 \text{ } \Omega \cdot \text{cm}^2$. The R_p of L2P1 was highest among those cells because the lower surface area of the larger ball-shaped LSC particles decrease reaction of oxygen ion diffusion, and power density is lowest though its high porosity. From those results, when the LSC and PVP were mixed with same weight ratio, LSC has better morphology and electrochemical performances.

Next, we confirmed the relation between solvent evaporation and the

morphology of the LSC layer. During ESD process, unevaporated solvents make more uniform film-like structure by leveling effect. But too much solvent droplets generate cracks and void during evaporation process. Therefore, we compared two kinds of solutions which are ethanol and ethanol/DI water mixture. The evaporation speed of DI water is much slower than ethanol, therefore we can confirm leveling effect and crack generation by different evaporation speed. Figure 4-6 shows structure of the annealed LSC dispersed in ethanol/DI water and ethanol mixture. From Figure 4-6a, bulk cracks is confirmed that LSC dispersed in ethanol/DI water mixture. Those cracks cause a fracture of LSC layer and decline of cathode performances. Peak power density of ethanol case were 401, 210 and 108 mW/cm², and ethanol/DI water mixture case were 287, 148, 96 mW/cm² at 650, 600 and 550 °C respectively. R_p of ethanol case were 1.7, 2.4 and 4.7 Ω · cm², and ethanol/DI water case were 2.7, 5.4 and 12 Ω · cm² at 650, 600 and 550 °C respectively. The performances and impedances of the ethanol case was better than the ethanol/DI water mixture one, and these differences comes from bulk cracks that impair reaction site of LSC.

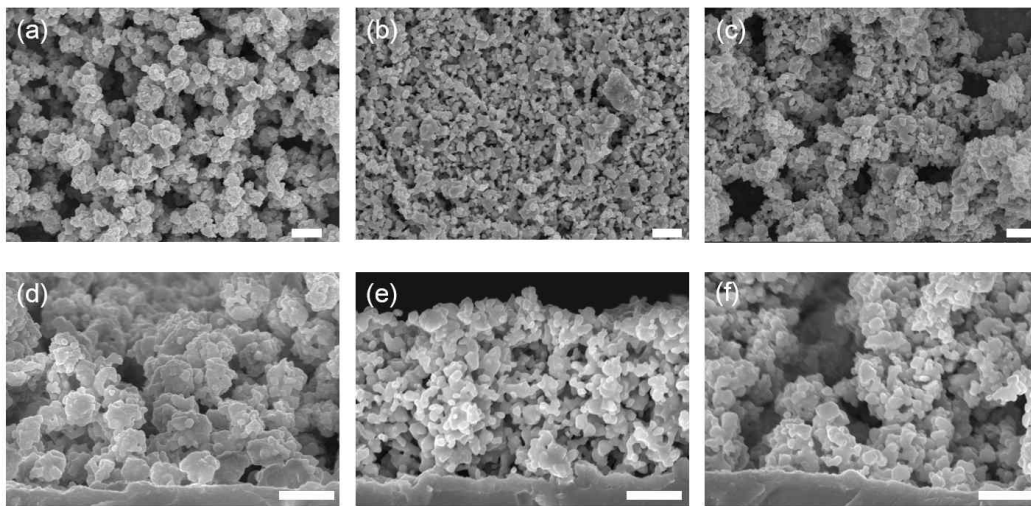


Fig 4-3. Planar (a)-(c) and Sectional (d)-(f) SEM images of the LSC cathode layer fabricated by ESD process under different weight ratio between LSC and PVP to solvent : (a) and (d) 10 : 5 (b) and (e) 10 : 10 (c) and (f) 10 : 20. Scale bars represent 2 μm in (a)-(c) and 1 μm in (d)-(f).

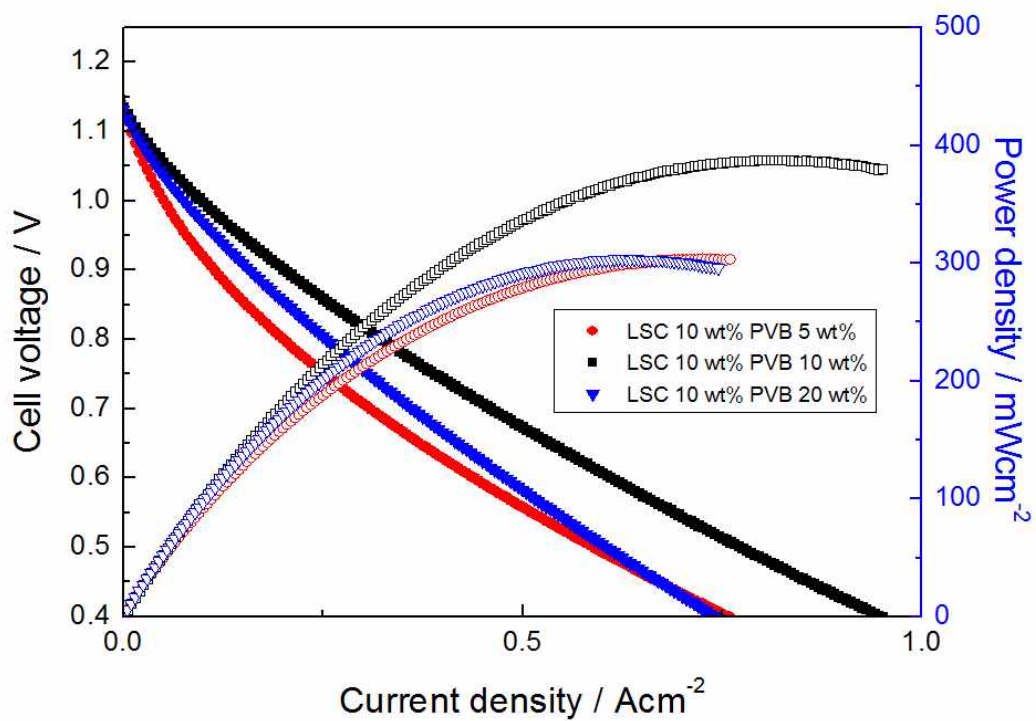


Figure 4-4. Electrochemical performances of LSC fabricated by ESD process with different PVP amount at 650 °C. (a) LSC : PVP = 10 : 5 (b) LSC : PVP = 10 : 10 (c) LSC : PVP = 10 : 20.

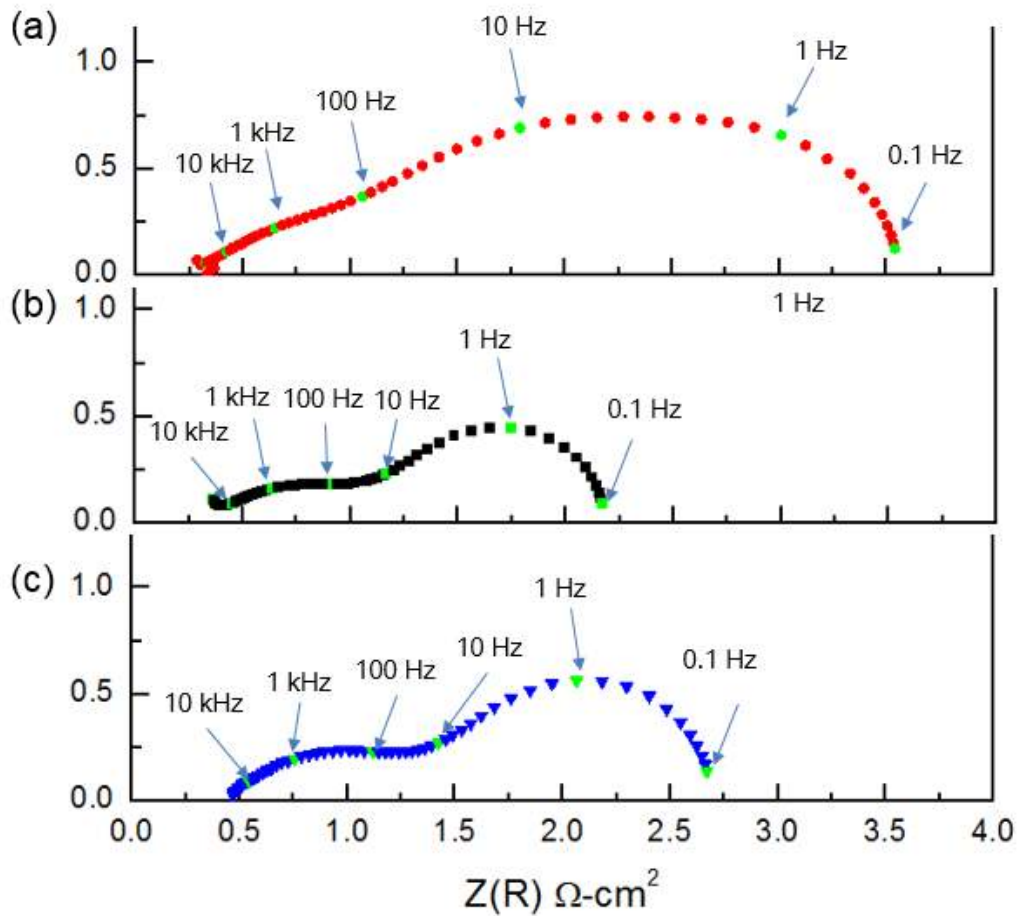


Figure 4-5. Impedance spectra results of LSC fabricated by ESD process with different PVP amount. All the impedance spectra was measured at OCV condition and 650 °C (a) LSC : PVP = 10 : 5 (b) LSC : PVP = 10 : 10 (c) LSC : PVP = 10 : 20.

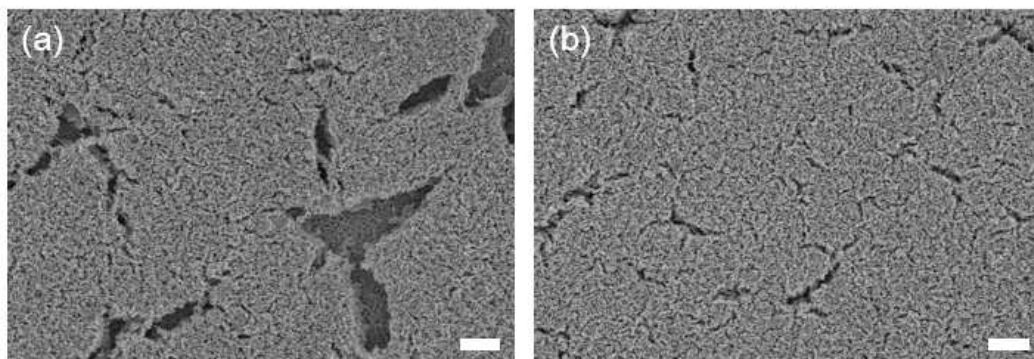


Figure 4-6. SEM images of deposited LSC by ESD process with different solvent conditions (a) Ethanol : DI water = 7 : 3 (b) Only ethanol.

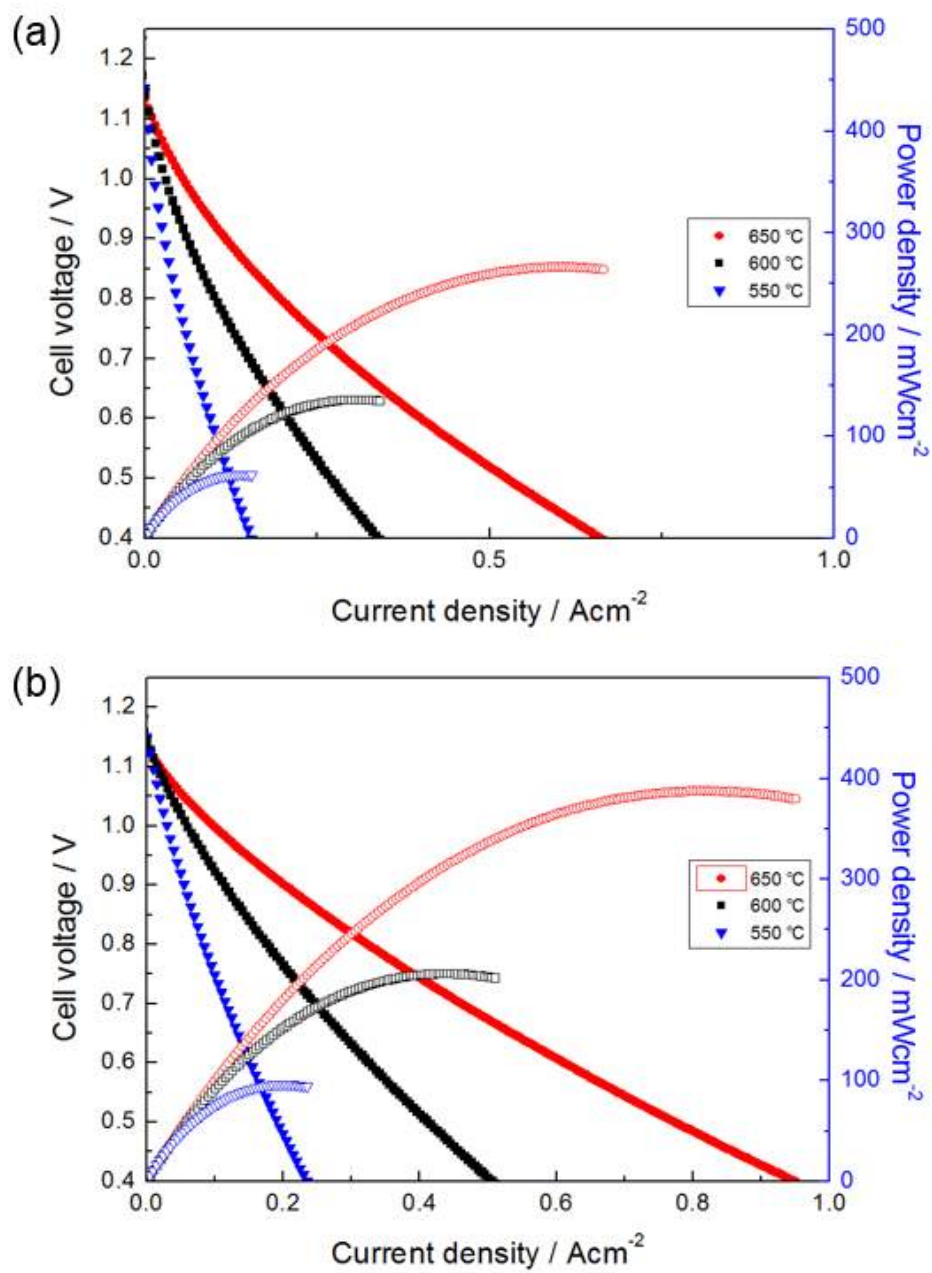


Figure 4-7. Electrochemical performances of LSC fabricated by ESD process. (a) Ethanol : DI water = 7 : 3 (b) Only ethanol.

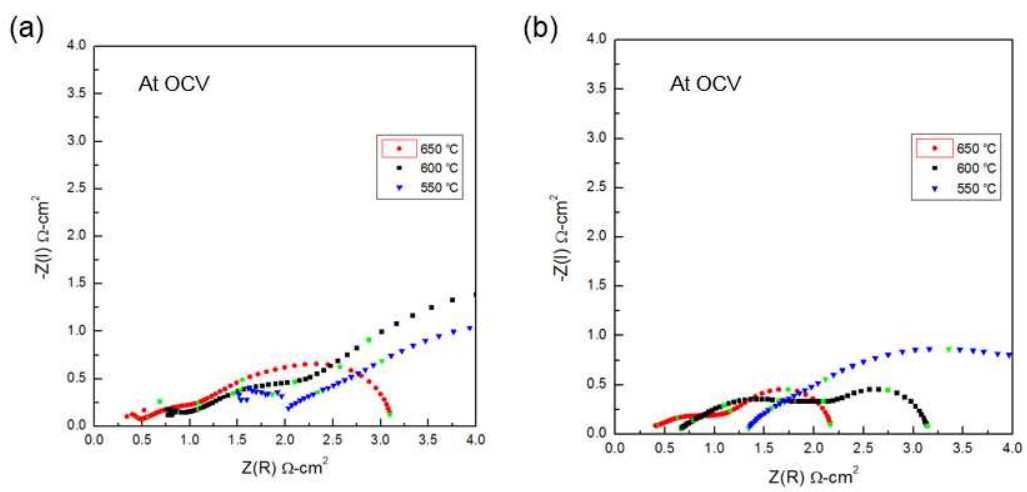


Figure 4-8. Impedance spectra of LSC fabricated by ESD process at 650 °C. (a) Ethanol : DI water = 7 : 3 (b) Only ethanol.

4-3-3. YSZ electrolyte deposition using electrospray deposition and structure control via polymer binder

In contrast to the cathode layer, the electrolyte has to form dense layer. Because the gas tightness which concludes OCV of the cell is influenced by this density of the electrolyte, if the leakage is occurred, the performance of the cell is decreased.

The dense structure of the electrolyte is formed during annealing process at 1400°C by crystallization of the YSZ particles. Because the NiO-YSZ substrate fabricated by pressing process have many micro size pore which bring about debonding problem, polymer binder become very important factor for dense electrolyte layer. Also the flow temperature of the binder has to be lower than 200°C, the temperature where the shrinkage of the substrate is started. For those reasons, we selected PVB as the binder polymer for the electrolyte deposition. The PVB has better adhesion than PVP and its flow temperature is lower as about 120°C.[86] During annealing process, sprayed PVB-YSZ composite rearranged at the flow temperature of the PVB, and this phenomena helps making uniform film layer. Therefore density of annealed YSZ structure is influenced by amount of the PVB polymer. When the content of the PVB is lower than the YSZ particle, they are crystallized with porous structure. Vice versa, the structure of the annealed electrolyte structure could be controlled via amount of the PVB polymer. Figure

4-3 shows the morphology change of deposited YSZ particle according to the different YSZ amount. In the PVB 2 wt% and YSZ 7 wt% case (figure 4-9a), YSZ particles make porous structure after sintering process because of lack of PVB which makes interconnection between the particles and dominates mass transportation. The porous structure transformed to membrane where small pores exist, as decrease of YSZ amount (Figure 4-9b). In the 2 wt% YSZ case, densely annealed electrolyte layer could be found. Figure 4-9c represents dense YSZ layer and porous AFL deposited by ESD process on the porous anode. It can be confirmed that the entirely dense YSZ is supported by AFL layer.

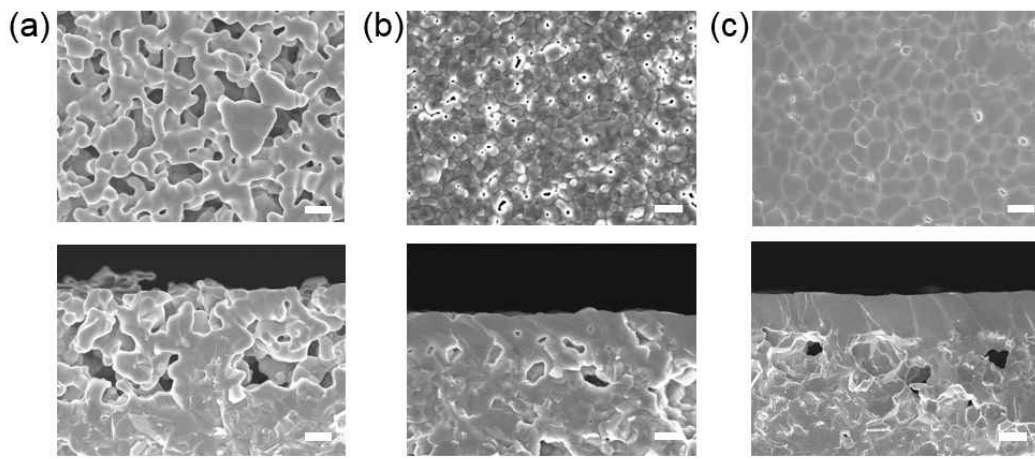


Figure 4-9. SEM images of YSZ layer deposited with different YSZ/PVB ratio: (a) 7 wt%/ 2 wt% (b) 4 wt% / 2 wt% (c) 2 wt%/2 wt%, scale bars represent 2 μm .

4-3-4. ESD Cell fabrication and its electrochemical performances

In the previous chapters, we show that the cathode and the electrolyte can be fabricated by only ESD and annealing process. Not only structure factor also electrochemical performances are very important to be used the component of the SOFC.

To fabricate efficiently dense and robust electrolyte layer, AFL which has 6:4 ratio of YSZ/NiO was screen printed followed by YSZ deposition. The AFL makes good adhesion between anode and electrolyte by reducing thermal mismatch and structural effect by anode substrate.[87, 88] The amount of YSZ were 2 wt% to the ethanol respectively and the PVB polymer was added with also 2 wt% to the ethanol. Then the same content of the GDC particles prevent sacrificing performance by the thermal fusion between LSC and YSZ were deposited with thin (<1 μm) layer. Then the CFL (GDC:LSC = 6:4) and LSC was deposited as same condition with Ch 4-3-2.

Two kinds of samples which have 2 μm and 4 μm thickness of YSZ were used to test their gas tightness property. Figure 4-10 shows cross-section SEM images of the cell fabricated by ESD process where dense YSZ layer and ~ 3 μm thickness of LSC cathode are deposited. When the YSZ is 2 μm , OCV of the cell was ~ 0.96 V (Figure 4-11a). It means 2 μm is not enough thickness for ESD-YSZ to prevent diffusion of gas molecules, and the cracks on electrolyte become the

reason of low electrochemical performance. But the OCV of the cell has 4 μm thickness of YSZ increased to ~ 1.13 V which is almost theoretical value. The peak power density of the cell have 4 μm YSZ was 660, 375 and 190 mW/cm^2 at 650, 600 and 550 $^{\circ}\text{C}$. All of the components could be fabricated successfully, and performances were not only better than other aerosol based methods [88-92], also results of the screen printed electrolyte cell in the previous chapter. R_{Ω} and R_p were decreased to 0.14 and 1.21 $\Omega\cdot\text{cm}^2$ because of the thinner electrolyte and optimized cathode structure. From these results, we could confirm that IT-SOFC can be successfully fabricated via our ESD method.

The ESD process has many advantages such as easy material preparation, fast, cost-effective and large area fabrication. Also combined conventional process, it can be made up for the weakness and have possibility for conjugating with various ways.

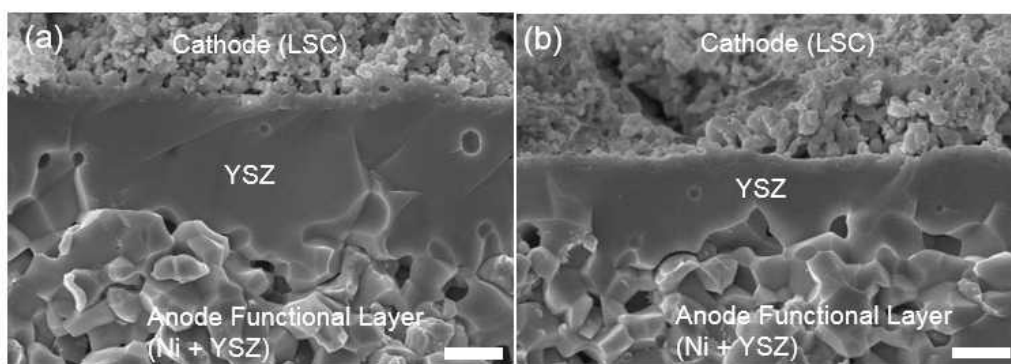


Figure 4-10. Cross-sectional SEM images of ESD cell. (a) 4 μm and (b) 2 μm thickness of YSZ. Scale bars represent 2 μm .

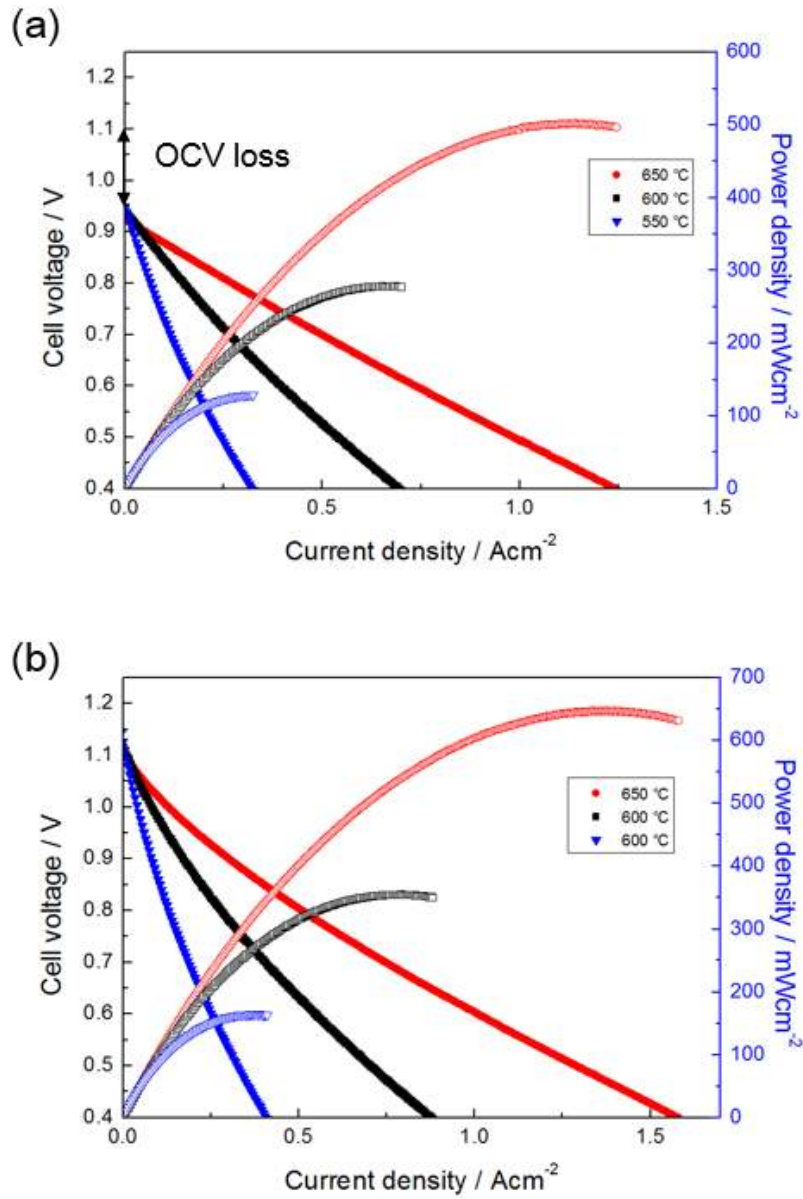


Figure 4-11. Electrochemical performances of cells fabricated by ESD process. 2 μm (a) and 4 μm (b) thickness of YSZ.

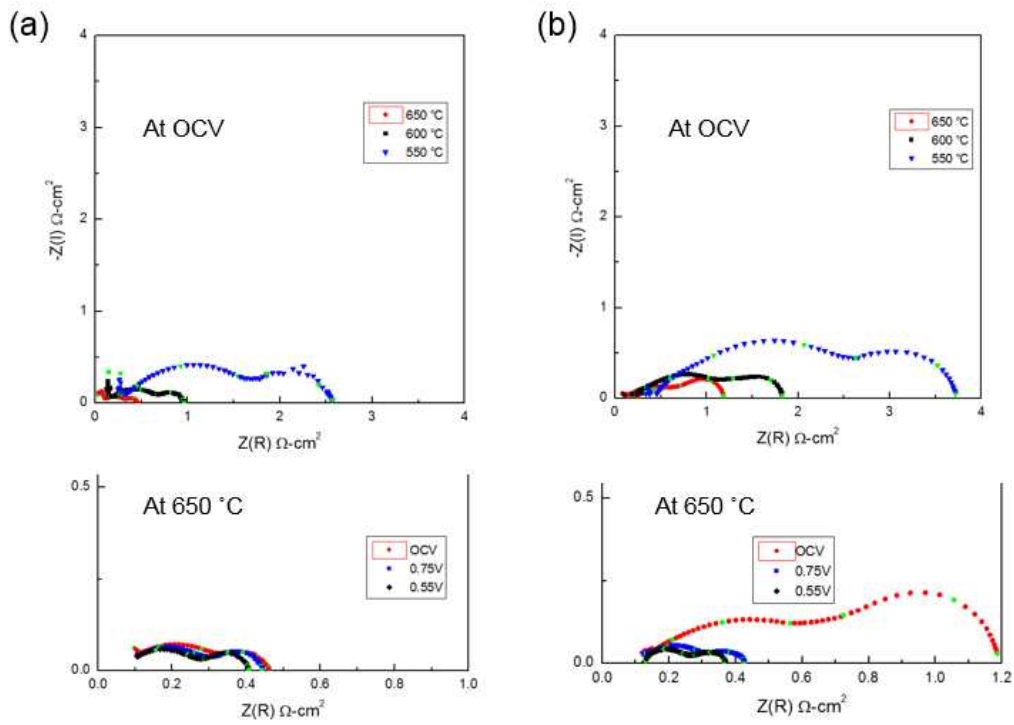


Figure 4-12. Impedance spectra results of the ESD cells fabricated by ESD process. 2 μm (a) and 4 μm (b) thickness of YSZ.

4-4. Summary

In this chapter, we have shown the fabrication of the components of SOFC via ESD process which has various advantages such as easy and fast process, uniform thin film deposition and structure controllable process. LSC cathode, YSZ electrolyte, GDC buffer layer and interlayers (AFL and CFL) could be deposited using electrospray method, it is shown that they can form working energy device.

Not only porous and thick cathode layer, also densely packed electrolyte could be fabricated using ESD and annealing process. Especially, we examined porosity of the cathode and electrolyte membrane can be controlled by amount of PVP and PVB polymer binder which affect mass transportation of ceramic nanoparticles. Also we optimized structures of those components through electrochemical analysis.

SOFC could be fabricated using ESD process or combining other process such as screen printing and PLD. The electrochemical performances of the cells were measured and it could be confirmed that those components work as energy conversion device. Furthermore, from structure and impedance analysis, we suggested possibilities of ESD process in fabrication of SOFC.

References

- [1] K. Autumn, Y. A. Liang, S. T. Hsieh, W. Zesch, W. P. Chan, T. W. Kenny, *et al.*, "Adhesive force of a single gecko foot-hair," *Nature*, vol. 405, pp. 681-685, Jun 8 2000.
- [2] J. B. Kim, P. Kim, N. C. Pegard, S. J. Oh, C. R. Kagan, J. W. Fleischer, *et al.*, "Wrinkles and deep folds as photonic structures in photovoltaics," *Nature Photonics*, vol. 6, pp. 327-332, May 2012.
- [3] H. Lee, B. P. Lee, and P. B. Messersmith, "A reversible wet/dry adhesive inspired by mussels and geckos," *Nature*, vol. 448, pp. 338-U4, Jul 19 2007.
- [4] H. E. Jeong, J. K. Lee, H. N. Kim, S. H. Moon, and K. Y. Suh, "A nontransferring dry adhesive with hierarchical polymer nanohairs," *Proceedings of the National Academy of Sciences of the United States of America*, vol. 106, pp. 5639-5644, Apr 7 2009.
- [5] P. J. Kelly and R. D. Arnell, "Magnetron sputtering: a review of recent developments and applications," *Vacuum*, vol. 56, pp. 159-172, Mar 2000.
- [6] M. Leskela and M. Ritala, "Atomic layer deposition (ALD): from precursors to thin film structures," *Thin Solid Films*, vol. 409, pp. 138-146, Apr 22 2002.
- [7] R. H. Tredgold, "An Introduction to Ultrathin Organic Films - from Langmuir-Blodgett to Self-Assembly - Ulman,A," *Nature*, vol. 354, p. 120-120, Nov 14 1991.
- [8] J. A. Franco, S. E. Kentish, J. M. Perera, and G. W. Stevens, "Fabrication of a superhydrophobic polypropylene membrane by deposition of a porous crystalline polypropylene coating," *Journal of Membrane Science*, vol. 318, pp. 107-113, Jun 20 2008.
- [9] J. H. Kim, G. M. Liu, and S. H. Kim, "Deposition of stable hydrophobic coatings with in-line CH₄ atmospheric rf plasma," *Journal of*

- Materials Chemistry*, vol. 16, pp. 977-981, 2006.
- [10] X. C. Dong, J. Chen, Y. W. Ma, J. Wang, M. B. Chan-Park, X. M. Liu, *et al.*, "Superhydrophobic and superoleophilic hybrid foam of graphene and carbon nanotube for selective removal of oils or organic solvents from the surface of water," *Chemical Communications*, vol. 48, pp. 10660-10662, 2012.
- [11] W. A. Daoud, J. H. Xin, Y. H. Zhang, and C. L. Mak, "Pulsed laser deposition of superhydrophobic thin Teflon films on cellulosic fibers," *Thin Solid Films*, vol. 515, pp. 835-837, Oct 25 2006.
- [12] Y. Liu, S. W. Zha, and M. L. Liu, "Novel nanostructured electrodes for solid oxide fuel cells fabricated by combustion chemical vapor deposition (CVD)," *Advanced Materials*, vol. 16, pp. 256+, Feb 3 2004.
- [13] X. R. Jiang, H. Huang, F. B. Prinz, and S. F. Bent, "Application of atomic layer deposition of platinum to solid oxide fuel cells," *Chemistry of Materials*, vol. 20, pp. 3897-3905, Jun 24 2008.
- [14] D. Perednis and L. J. Gauckler, "Solid oxide fuel cells with electrolytes prepared via spray pyrolysis," *Solid State Ionics*, vol. 166, pp. 229-239, Jan 2004.
- [15] E. O. Oh, C. M. Whang, Y. R. Lee, S. Y. Park, D. H. Prasad, K. J. Yoon, *et al.*, "Fabrication of thin-film gadolinia-doped ceria (GDC) interdiffusion barrier layers for intermediate-temperature solid oxide fuel cells (IT-SOFCs) by chemical solution deposition (CSD)," *Ceramics International*, vol. 40, pp. 8135-8142, Jul 2014.
- [16] !!! INVALID CITATION !!!
- [17] A. Olah, H. Hillborg, and G. J. Vancso, "Hydrophobic recovery of UV/ozone treated poly(dimethylsiloxane): adhesion studies by contact mechanics and mechanism of surface modification," *Applied Surface Science*, vol. 239, pp. 410-423, Jan 31 2005.
- [18] B. Sanii and A. N. Parikh, "Patterning fluid and elastomeric surfaces using short-wavelength UV radiation and photogenerated reactive ox

- xygen species," *Annual Review of Physical Chemistry*, vol. 59, pp. 411-432, 2008.
- [19] Z. J. Zheng, O. Azzaroni, F. Zhou, and W. T. S. Huck, "Topography printing to locally control wettability," *Journal of the American Chemical Society*, vol. 128, pp. 7730-7731, Jun 21 2006.
- [20] P. Kim, R. Kwak, S. H. Lee, and K. Y. Suh, "Solvent-Assisted Decal Transfer Lithography by Oxygen-Plasma Bonding and Anisotropic Swelling," *Advanced Materials*, vol. 22, pp. 2426-+, Jun 11 2010.
- [21] Y. K. Kim, G. T. Kim, and J. S. Ha, "Simple patterning via adhesion between a buffered-oxide etchant-treated PDMS stamp and a SiO₂ substrate," *Advanced Functional Materials*, vol. 17, pp. 2125-2132, Sep 3 2007.
- [22] A. L. Thangawng, M. A. Swartz, M. R. Glucksberg, and R. S. Ruoff, "Bond-detach lithography: A method for micro/nanolithography by precision PDMS patterning," *Small*, vol. 3, pp. 132-138, Jan 2007.
- [23] W. R. Childs and R. G. Nuzzo, "Large-area patterning of coinage-metal thin films using decal transfer lithography," *Langmuir*, vol. 21, pp. 195-202, Jan 4 2005.
- [24] J. Y. Park, S. J. Yoo, E. J. Lee, D. H. Lee, J. Y. Kim, and S. H. Lee, "Increased poly(dimethylsiloxane) stiffness improves viability and morphology of mouse fibroblast cells," *Biochip Journal*, vol. 4, pp. 230-236, Sep 20 2010.
- [25] Q. T. Nguyen, Z. Bendjama, R. Clement, and Z. H. Ping, "Poly(dimethylsiloxane) crosslinked in different conditions Part I. Sorption properties in water-ethyl acetate mixtures," *Physical Chemistry Chemical Physics*, vol. 1, pp. 2761-2766, Jun 1 1999.
- [26] D. Fuard, T. Tzvetkova-Chevolleau, S. Decossas, P. Tracqui, and P. Schiavone, "Optimization of poly-di-methyl-siloxane (PDMS) substrates for studying cellular adhesion and motility," *Microelectronic Engineering*, vol. 85, pp. 1289-1293, May-Jun 2008.
- [27] A. Amirsadeghi, J. J. Lee, and S. Park, "A Simulation Study on the

- Effect of Cross-Linking Agent Concentration for Defect Tolerant Demolding in UV Nanoimprint Lithography," *Langmuir*, vol. 28, pp. 11546-11554, Aug 7 2012.
- [28] *Fracture nanomechanics*. Singapore: Pan Stanford Pub., 2011.
- [29] W. R. Childs and R. G. Nuzzo, "Decal transfer microlithography: A new soft-lithographic patterning method," *Journal of the American Chemical Society*, vol. 124, pp. 13583-13596, Nov 13 2002.
- [30] H. Hillborg, J. F. Ankner, U. W. Gedde, G. D. Smith, H. K. Yasuda, and K. Wikstrom, "Crosslinked polydimethylsiloxane exposed to oxygen plasma studied by neutron reflectometry and other surface specific techniques," *Polymer*, vol. 41, pp. 6851-6863, Aug 2000.
- [31] T. Suni, K. Henttinen, I. Suni, and J. Mäkinen, "Effects of plasma activation on hydrophilic bonding of Si and SiO₂," *Journal of the Electrochemical Society*, vol. 149, pp. G348-G351, Jun 2002.
- [32] J. Y. Park, H. Y. Chae, C. H. Chung, S. J. Sim, J. Park, H. H. Lee, *et al.*, "Controlled wavelength reduction in surface wrinkling of poly(dimethylsiloxane)," *Soft Matter*, vol. 6, pp. 677-684, 2010.
- [33] M. Pretzl, A. Schweikart, C. Hanske, A. Chiche, U. Zettl, A. Horn, *et al.*, "A Lithography-Free Pathway for Chemical Microstructuring of Macromolecules from Aqueous Solution Based on Wrinkling," *Langmuir*, vol. 24, pp. 12748-12753, Nov 18 2008.
- [34] A. A. Volinsky, N. R. Moody, and W. W. Gerberich, "Interfacial toughness measurements for thin films on substrates," *Acta Materialia*, vol. 50, pp. 441-466, Feb 8 2002.
- [35] K. Efimenko, W. E. Wallace, and J. Genzer, "Surface modification of Sylgard-184 poly(dimethyl siloxane) networks by ultraviolet and ultraviolet/ozone treatment," *Journal of Colloid and Interface Science*, vol. 254, pp. 306-315, Oct 15 2002.
- [36] D. Bodas and C. Khan-Malek, "Formation of more stable hydrophilic surfaces of PDMS by plasma and chemical treatments," *Microelectronic Engineering*, vol. 83, pp. 1277-1279, Apr-Sep 2006.

- [37] R. M. Lycans, C. B. Higgins, M. S. Tanner, E. R. Blough, and B. S. Day, "Plasma treatment of PDMS for applications of in vitro motility assays," *Colloids and Surfaces B-Biointerfaces*, vol. 116, pp. 687-694, Apr 1 2014.
- [38] M. Abdelmouleh, S. Boufi, M. N. Belgacem, A. P. Duarte, A. Ben Salah, and A. Gandini, "Modification of cellulosic fibres with functionalised silanes: development of surface properties," *International Journal of Adhesion and Adhesives*, vol. 24, pp. 43-54, Feb 2004.
- [39] J. J. Yoo and S. H. Rhee, "Evaluations of bioactivity and mechanical properties of poly (epsilon-caprolactone) silica nanocomposite following heat treatment," *Journal of Biomedical Materials Research Part A*, vol. 68A, pp. 401-410, Mar 1 2004.
- [40] H. H. H. Shi, J. Bao, J. Im, P. S. Ho, Y. Zhou, J. T. Pender, M. Armacost, and D. Kyser, " Plasma Altered Layer Model for Plasma Damage Characterization of Porous OSG Films," *Proceedings of the IEEE International Interconnect Technology Conference* p. 78., 2009.
- [41] J. H. Lee, Y. M. Lee, Y. H. Kim, J. Y. Lee, S. J. Choi, and P. J. Yoo, "Liquid-Liquid Interfacial Nanomolding," *Small*, vol. 7, pp. 2587-2592, Sep 19 2011.
- [42] V. P. Shantarovich, I. B. Kevdina, Y. P. Yampolskii, and A. Y. Alentiev, "Positron annihilation lifetime study of high and low free volume glassy polymers: Effects of free volume sizes on the permeability and permselectivity," *Macromolecules*, vol. 33, pp. 7453-7466, Oct 3 2000.
- [43] Y. Z. Ding, S. Garland, M. Howland, A. Revzin, and T. R. Pan, "Universal Nanopatternable Interfacial Bonding," *Advanced Materials*, vol. 23, pp. 5551-+, Dec 8 2011.
- [44] G. Altankov, T. Groth, N. Krasteva, W. Albrecht, and D. Paul, "Morphological evidence for a different fibronectin receptor organization and function during fibroblast adhesion on hydrophilic and hydrophobic glass substrata," *Journal of Biomaterials Science-Polymer Edition*,

- vol. 8, pp. 721-740, 1997.
- [45] H. U. Lee, S. Y. Park, Y. H. Kang, S. Y. Jeong, S. H. Choi, K. Y. Jahng, *et al.*, "Surface modification of and selective protein attachment to a flexible microarray pattern using atmospheric plasma with a reactive gas," *Acta Biomaterialia*, vol. 6, pp. 519-525, Feb 2010.
- [46] J. D. Hoff, L. J. Cheng, E. Meyhofer, L. J. Guo, and A. J. Hunt, "Nanoscale protein patterning by imprint lithography," *Nano Letters*, vol. 4, pp. 853-857, May 2004.
- [47] W. Senaratne, P. Sengupta, V. Jakubek, D. Holowka, C. K. Ober, and B. Baird, "Functionalized surface arrays for spatial targeting of immune cell signaling," *Journal of the American Chemical Society*, vol. 128, pp. 5594-5595, May 3 2006.
- [48] L. M. Demers, D. S. Ginger, S. J. Park, Z. Li, S. W. Chung, and C. A. Mirkin, "Direct patterning of modified oligonucleotides on metals and insulators by dip-pen nanolithography," *Science*, vol. 296, pp. 1836-1838, Jun 7 2002.
- [49] X. Yao, J. Ju, S. Yang, J. J. Wang, and L. Jiang, "Temperature-Driven Switching of Water Adhesion on Organogel Surface," *Advanced Materials*, vol. 26, pp. 1895-1900, Mar 2014.
- [50] C. M. Chen and S. Yang, "Directed Water Shedding on High-Aspect-Ratio Shape Memory Polymer Micropillar Arrays," *Advanced Materials*, vol. 26, pp. 1283-1288, Feb 2014.
- [51] A. Grigoryev, T. Tokarey, K. G. Kornev, I. Luzinov, and S. Minko, "Superomniphobic Magnetic Microtextures with Remote Wetting Control," *Journal of the American Chemical Society*, vol. 134, pp. 12916-12919, Aug 8 2012.
- [52] J. Ju, H. Bai, Y. M. Zheng, T. Y. Zhao, R. C. Fang, and L. Jiang, "A multi-structural and multi-functional integrated fog collection system in cactus," *Nature Communications*, vol. 3, Dec 2012.
- [53] L. Feng, Y. A. Zhang, J. M. Xi, Y. Zhu, N. Wang, F. Xia, *et al.*, "Petal effect: A superhydrophobic state with high adhesive force," *La*

- ngmuir*, vol. 24, pp. 4114-4119, Apr 15 2008.
- [54] L. Zhai, M. C. Berg, F. C. Cebeci, Y. Kim, J. M. Milwid, M. F. Rubner, *et al.*, "Patterned superhydrophobic surfaces: Toward a synthetic mimic of the Namib Desert beetle," *Nano Letters*, vol. 6, pp. 1213-1217, Jun 2006.
- [55] K. H. Chu, R. Xiao, and E. N. Wang, "Uni-directional liquid spreading on asymmetric nanostructured surfaces," *Nature Materials*, vol. 9, pp. 413-417, May 2010.
- [56] N. A. Malvadkar, M. J. Hancock, K. Sekeroglu, W. J. Dressick, and M. C. Demirel, "An engineered anisotropic nanofilm with unidirectional wetting properties," *Nature Materials*, vol. 9, pp. 1023-1028, Dec 2010.
- [57] D. Y. Xia, L. M. Johnson, and G. P. Lopez, "Anisotropic Wetting Surfaces with One-Dimensional and Directional Structures: Fabrication Approaches, Wetting Properties and Potential Applications," *Advanced Materials*, vol. 24, pp. 1287-1302, Mar 8 2012.
- [58] G. Azimi, R. Dhiman, H. M. Kwon, A. T. Paxson, and K. K. Varanasi, "Hydrophobicity of rare-earth oxide ceramics," *Nature Materials*, vol. 12, pp. 315-320, Apr 2013.
- [59] A. Grigoryev, Y. Roiter, I. Tokarev, I. Luzinov, and S. Minko, "Colloidal Occlusion Template Method for Micromanufacturing of Omnipotent Surfaces," *Advanced Functional Materials*, vol. 23, pp. 870-877, Feb 18 2013.
- [60] Y. C. Jung and B. Bhushan, "Contact angle, adhesion and friction properties of micro- and nanopatterned polymers for superhydrophobicity," *Nanotechnology*, vol. 17, pp. 4970-4980, Oct 14 2006.
- [61] S. M. Kang, C. Lee, H. N. Kim, B. J. Lee, J. E. Lee, M. K. Kwak, *et al.*, "Directional Oil Sliding Surfaces with Hierarchical Anisotropic Groove Microstructures," *Advanced Materials*, vol. 25, pp. 5756+, Oct 2013.
- [62] J. D. Smith, R. Dhiman, S. Anand, E. Reza-Garduno, R. E. Cohen,

- G. H. McKinley, *et al.*, "Droplet mobility on lubricant-impregnated surfaces," *Soft Matter*, vol. 9, pp. 1772-1780, 2013.
- [63] X. Yao, Y. H. Hu, A. Grinthal, T. S. Wong, L. Mahadevan, and J. Aizenberg, "Adaptive fluid-infused porous films with tunable transparency and wettability," *Nature Materials*, vol. 12, pp. 529-534, Jun 2013.
- [64] D. M. Drotlef, P. Blumler, and A. del Campo, "Magnetically Actuated Patterns for Bioinspired Reversible Adhesion (Dry and Wet)," *Advanced Materials*, vol. 26, pp. 775-779, Feb 5 2014.
- [65] S. J. Choi, K. Y. Suh, and H. H. Lee, "A geometry controllable approach for the fabrication of biomimetic hierarchical structure and its superhydrophobicity with near-zero sliding angle," *Nanotechnology*, vol. 19, Jul 9 2008.
- [66] S. M. Kang, S. M. Kim, H. N. Kim, M. K. Kwak, D. H. Tahk, and K. Y. Suh, "Robust superomniphobic surfaces with mushroom-like micropillar arrays," *Soft Matter*, vol. 8, pp. 8563-8568, 2012.
- [67] C. I. Park, H. E. Jeong, S. H. Lee, H. S. Cho, and K. Y. Suh, "Wetting transition and optimal design for microstructured surfaces with hydrophobic and hydrophilic materials," *Journal of Colloid and Interface Science*, vol. 336, pp. 298-303, Aug 1 2009.
- [68] A. B. D. Cassie and S. Baxter, "Wettability of porous surfaces," *Transactions of the Faraday Society*, vol. 40, pp. 0546-0550, 1944.
- [69] R. N. Wenzel, "Resistance of solid surfaces to wetting by water," *Industrial and Engineering Chemistry*, vol. 28, pp. 988-994, 1936.
- [70] H. E. Jeong, M. K. Kwak, C. I. Park, and K. Y. Suh, "Wettability of nanoengineered dual-roughness surfaces fabricated by UV-assisted capillary force lithography," *Journal of Colloid and Interface Science*, vol. 339, pp. 202-207, Nov 1 2009.
- [71] M. Naya, I. Tsuruma, T. Tani, A. Mukai, S. Sakaguchi, and S. Yasunami, "Near-field optical photolithography for high-aspect-ratio patterning using bilayer resist," *Applied Physics Letters*, vol. 86, May 16

2005.

- [72] A. L. Bogdanov and S. S. Peredkov, "Use of SU-8 photoresist-for very high aspect ratio x-ray lithography," *Microelectronic Engineering*, vol. 53, pp. 493-496, Jun 2000.
- [73] H. Liu, B. Wang, L. Ke, J. Deng, C. C. Chum, S. L. Teo, *et al.*, "High Aspect Subdiffraction-Limit Photolithography via a Silver Super lens," *Nano Letters*, vol. 12, pp. 1549-1554, Mar 2012.
- [74] Y. Y. Zhu, D. S. Antao, R. Xiao, and E. N. Wang, "Real-Time Manipulation with Magnetically Tunable Structures," *Advanced Materials*, vol. 26, pp. 6442-6446, Oct 8 2014.
- [75] F. Khademolhosseini and M. Chiao, "Fabrication and Patterning of Magnetic Polymer Micropillar Structures Using a Dry-Nanoparticle Embedding Technique," *Journal of Microelectromechanical Systems*, vol. 22, pp. 131-139, Feb 2013.
- [76] N. J. Sniadecki, A. Anguelouch, M. T. Yang, C. M. Lamb, Z. Liu, S. B. Kirschner, *et al.*, "Magnetic microposts as an approach to apply forces to living cells," *Proceedings of the National Academy of Sciences of the United States of America*, vol. 104, pp. 14553-14558, Sep 11 2007.
- [77] H. E. Jeong, S. H. Lee, J. K. Kim, and K. Y. Suh, "Nanoengineered multiscale hierarchical structures with tailored wetting properties," *Langmuir*, vol. 22, pp. 1640-1645, Feb 14 2006.
- [78] D. M. Drotlef, P. Blumler, P. Papadopoulos, and A. del Campo, "Magnetically Actuated Micropatterns for Switchable Wettability," *Acs Applied Materials & Interfaces*, vol. 6, pp. 8702-8707, Jun 11 2014.
- [79] H. S. Noh, K. J. Yoon, B. K. Kim, H. J. Je, H. W. Lee, J. H. Lee, *et al.*, "The potential and challenges of thin-film electrolyte and nanostructured electrode for yttria-stabilized zirconia-base anode-supported solid oxide fuel cells," *Journal of Power Sources*, vol. 247, pp. 105-111, Feb 1 2014.
- [80] Y. H. Gong, D. Palacio, X. Y. Song, R. L. Patel, X. H. Liang, X.

- Zhao, *et al.*, "Stabilizing Nanostructured Solid Oxide Fuel Cell Cathode with Atomic Layer Deposition," *Nano Letters*, vol. 13, pp. 4340-4345, Sep 2013.
- [81] M. Cassir, A. Ringuede, and L. Niinisto, "Input of atomic layer deposition for solid oxide fuel cell applications," *Journal of Materials Chemistry*, vol. 20, pp. 8987-8993, 2010.
- [82] W. E. Teo and S. Ramakrishna, "A review on electrospinning design and nanofibre assemblies," *Nanotechnology*, vol. 17, pp. R89-R106, Jul 28 2006.
- [83] A. Jaworek and A. T. Sobczyk, "Electrospraying route to nanotechnology: An overview," *Journal of Electrostatics*, vol. 66, pp. 197-219, Mar 2008.
- [84] I. B. Rietveld, K. Kobayashi, H. Yamada, and K. Matsushige, "Electrospray deposition, model, and experiment: Toward general control of film morphology," *Journal of Physical Chemistry B*, vol. 110, pp. 23351-23364, Nov 23 2006.
- [85] S. J. Skinner, "Recent advances in Perovskite-type materials for solid oxide fuel cell cathodes," *International Journal of Inorganic Materials*, vol. 3, pp. 113-121, Mar 2001.
- [86] R. K. Jena, X. Chen, C. Y. Yue, and Y. C. Lam, "Viscosity of COC polymer (TOPAS) near the glass transition temperature: Experimental and modeling," *Polymer Testing*, vol. 29, pp. 933-938, Dec 2010.
- [87] Z. H. Wang, N. Q. Zhang, J. S. Qiao, K. N. Sun, and P. Xu, "Improved SOFC performance with continuously graded anode functional layer," *Electrochemistry Communications*, vol. 11, pp. 1120-1123, Jun 2009.
- [88] S. Y. Park, H. I. Ji, H. R. Kim, K. J. Yoon, J. W. Son, B. K. Kim, *et al.*, "Structural optimization of (La, Sr)CoO₃-based multilayered composite cathode for solid-oxide fuel cells," *Journal of Power Sources*, vol. 228, pp. 97-103, Apr 15 2013.
- [89] R. P. Reolon, C. M. Halmenschlager, R. Neagu, C. D. Malfatti, and

- C. P. Bergmann, "Electrochemical performance of gadolinia-doped ceria (CGO) electrolyte thin films for ITSOFC deposited by spray pyrolysis," *Journal of Power Sources*, vol. 261, pp. 348-355, Sep 1 2014.
- [90] S. H. Choi, S. W. Kim, C. S. Hwang, and M. H. Lee, "Freestanding Micro-SOFCs with Electrodes Prepared by Electrostatic Spray Deposition," *Fuel Cells*, vol. 14, pp. 332-335, Apr 2014.
- [91] H. Nomura, S. Parekh, J. R. Selmán, and S. Al-Hallaj, "Fabrication of YSZ electrolyte for intermediate temperature solid oxide fuel cell using electrostatic spray deposition: II - Cell performance," *Journal of Applied Electrochemistry*, vol. 35, pp. 1121-1126, Nov 2005.
- [92] O. Wilhelm, S. E. Pratsinis, D. Perednis, and L. J. Gauckler, "Electrospray and pressurized spray deposition of yttria-stabilized zirconia films," *Thin Solid Films*, vol. 479, pp. 121-129, May 23 2005.

국문초록

본 학위 논문에서는 멀티스케일 증착 공정을 이용하여 다양한 기능성 표면을 제작하기 위한 방법을 제시하고 그 결과에 대해 기술하였다. 자연계에는 건식접착, 초소수성 표면, 마찰 감소, 에너지 생산과 같은 다양한 기능을 가진 표면 구조들이 무수히 존재한다. 이러한 구조들은 오랜 세월 동안 주위환경에 적응하여 최적화 된 형태를 가진다. 그 동안 많은 과학자들이 이러한 구조의 특성을 밝히고 그 기능을 모사하기 위한 연구를 진행해왔고, 그 결과 회전도포, 화학기상증착법 (CVD), 물리적기상증착법(PLD), 원자층증착법(ALD) 과 같은 다양한 표면증착 기술들이 개발되어 기능성 표면 제작을 위한 다양한 응용을 가능케 하였다. 이러한 공정들은 정밀하고 다양한 재료들을 증착 할 수 있는 장점이 있는 동시에 재료 물질의 제작과 느린 공정시간, 진공 및 고온 공정이 필요한 단점을 가진다. 본 논문에서는 상기 공정의 단점을 보완하고, 새로운 기능성 표면 제작을 위한 멀티스케일 증착 공정을 제안하였다.

먼저, 고분자 물질의 표면 개질 및 탄성 불균형 현상을 이용해 소수성의 나노두께 박막을 제작할 수 있는 연구를 진행하였다. 산소 플라즈마가 처리된 Poldimethylsiloxane (PDMS) 고분자는 표면에 100 nm 이하의 산화막을 형성하게 된다. 이 때 표면에는 친수성의 -OH 작용기가 만들어지게 되고 이는 열처리를 통해 같은 작용기를 가진

기판과 비가역적인 강한 결합을 하게 된다. 이러한 결합 하에서 수직응력이 가해지게 되면 PDMS 와 플라즈마 처리를 통해 변화된 산화막 사이의 탄성 불균형에 의해 계면에 응력이 집중되고, 계면을 따라 파단면이 생성되어 얇은 산화막이 기판에 전사되게 된다. 본 공정은 동일한 고분자 조각으로 10 회 이상 반복이 가능하며 표면 특성도 동일함을 확인 할 수 있었다. 전사된 나노박막은 접촉각 110° 이상의 소수성질을 가짐으로써 플라즈마 처리가 된 주변 기판과 구분되는 특성을 가지는 것을 알 수 있다. 또한 마이크로/나노 구조를 가지는 PDMS 몰드로 같은 공정을 진행 한 경우 그 모양이 그대로 전사되는 것을 확인함으로써 구조를 가지는 박막의 전사가 가능한 결과를 보였다. 이러한 공정으로 제작된 마이크로 웰(well) 구조는 내부의 표면은 친수성질을 가지고 벽면은 소수성질을 가지게 되므로 웰 내부에만 단백질의 고정이 가능하였다. 단백질간의 면역반응과 형광 이미지를 이용해 800 nm 지름의 웰 구조에 성공적으로 단백질의 패터닝이 가능한 것을 확인하였고, 이는 대면적의 기판에 복잡한 형상의 나노 박막을 빠르게 제작이 가능한 장점을 가진다. 본 결과는 고분자 나노박막의 새로운 증착 방법과 그 활용방법을 제시한 의미가 있다.

다음으로는 능동적 움직임이 가능한 초소수성 섬모에 대한 연구를 진행하였다. 이전의 결과에서 나노박막 패턴을 이용해 고정되어 있는

형상으로 젖음 특성을 조절하였다면, 본 연구는 외부의 자극에 반응 할 수 있는 자성 복합구조를 이용하여 능동적으로 표면 특성이 가능한 결과를 보였다. 자성을 가지는 철 입자를 반응입자로 사용하였고 PDMS 고분자가 지지체로 이용되었다. 두 물질을 헥세인(Hexane)에 같은 비율로 넣고 초음파분산기를 사용하여 균일하게 분산하였다. 그리고 압력분사방식을 이용하여 혼합용액을 도포하게 되는데, 이때 기관의 아래에 네오디뮴 자석을 이용하여 자기장이 존재하는 상태를 만들어주었다. 분사된 용액은 자기장의 방향을 따라 정렬됨으로써 고종횡비의 섬모구조를 만들게 되고, 탄소나노입자를 뒤이어 도포함으로써 150° 이상의 접촉각을 가지는 멀티스케일 초소수성 제작 할 수 있었다. 본 연구에서는 자기장의 세기와 용액의 도포 양 및 횡수에 따른 섬모 구조의 변화와 그에 따른 초소수성 성질의 변화를 관찰하였다. 제작된 섬모는 외부 자기장에 의해 변형이 가능하였으며 이를 이용해 액적의 흐름 방향 및 움직임은 즉각적으로 제어할 수 있었다. 또한 저온 환경에서 섬모 표면에 발생하는 얼음입자들을 섬모 자체의 움직임을 통해 제거 가능함을 보임으로써 다양한 응용이 가능한 초소수성 섬모의 새로운 제작 방법을 제안하였다.

마지막으로, 전기분사증착(Electrospray deposition, ESD) 공정을 이용하여 고체산화물연료전지(Solid Oxide Fuel Cell, SOFC)의 요소들을 증착하고, 이를 통해 하나의 소자로서 작동 가능한 셀을 제작하였다.

전기분사 공정은 압력분사공정에 비해 미세구조의 형성 및 형상 조절이 용이하여 수 입자 수준의 증착이 가능한 장점을 가진다. 또한 고분자 바인더의 함량에 따라 입자간의 연결구조가 달라지므로 다공성의 구조와 밀한 박막 구조를 각각 제작 가능한 특성이 있다. 이러한 특징을 이용하여 넓은 반응면적을 얻기 위한 다공성의 양극과 기체의 투과를 막기 위한 밀한 구조의 전해질 박막을 제작할 수 있었다. 특히, 고분자 바인더로 사용된 polyvinylbutyral(PVB)의 양이 늘어남에 따라 소결후의 전해질의 구조가 다공성의 구조에서 밀한 구조로 변화해 가는 것을 확인할 수 있었다. 전기분사공정을 기존의 공정과 연계하여 스크린 프린팅 공정으로 제작된 NiO-YSZ 기판 및 전해질 상에 양극을 여러 가지 조건으로 증착 하여 형상에 따른 전기적 특성을 측정하였고, 이를 통해 최적화된 양극 증착 조건을 확립할 수 있었다. 또한 전기분사 공정만으로 제작된 소자에서도 650 °C 에서 660 mW/cm² 의 결과를 얻을 수 있었다.

주요어: 기능성 표면, 증착 공정, 탄성 불균형, 초소수성 표면, 자성 복합체, 능동성 고분자 구조, 고체산화물 연료전지, 전기분사증착 공정

학번: 2009-23907